Organic free montmorillonite-based flexible insulating sheaths for Nb₃Sn superconductor magnets.

Eric Prouzet,[1]* Alexandre Puigségur,[2,3] André Larbot,[2] Jean-Michel Rey,[3] Françoise Rondeaux[3]

[1] University of Waterloo, Chemistry Dept & WIN 200 University Av. W (ON) N2L 3G1 (Canada)

[2] European Institute of Membrane (University Montpellier, - CNRS – ENSCM), CNRS, 1919 Route de Mende, 34293 Montpellier (France)

[3] CEA Saclay, DSM/IRFU/SACM/LEAS, F-91191, Gif-Sur-Yvette (France)

TITLE RUNNING HEAD. An organic free ceramic sheath was prepared by combining montmorillonite with a low temperature frit and glass ribbons. The resulting ribbon is plastic in its dried state, and sinter at low temperature (600-700°C) under inert atmosphere. This sheath was used for the manufacturing of Nb₃Sn superconducting magnets.

Fax: +1 519 746-0435; tel: +1 519 888-4567 x38172; e-mail: eprouzet@uwaterloo.ca

ABSTRACT. Nb_3Sn is a superconductor that exhibits higher performances than NbTi alloy currently used in superconducting magnets, regarding both the critical magnetic field and critical current. However, Nb_3Sn is an intermetallic compound prepared by thermal treatment, which loses ductility and plasticity once reacted. Since organic materials cannot be used as insulating sheaths and applied before the thermal treatment required for the synthesis of Nb_3Sn, a clay mineral-based organic-free sheath was prepared, which can be applied to Nb_3Sn magnetic coils prepared by the wind & react method, before the thermal process. This process allows for facile shaping of the superconductor precursor, before reaction, along with the application of the insulating coating, the sintering of this coating being achieved by the thermal treatment required for the synthesis of Nb_3Sn. This process has been designed for industrial developments and facile scale-up. The final material is an organic-free ceramic ribbon that can be stored before further use as an insulating sheath of Nb_3Sn wires, and electrical and magnetic tests on both the material and a specific demonstrator made with a 20 m superconducting reel, demonstrate that this material can be used as an insulating sheath, with no side-effect on superconductor properties.

1. Introduction

1.1. General background

Large research programs have been initiated within the last years to expand the technology of high field dipole magnets, especially for the future upgrade of the Large Hadron Collider (LHC) (Devred et al., 2004; Devred et al., 2006; Canfer et al., 2008; Loveridge et al., 2008). In this domain, scientific, engineering and industrial challenges are taken to their apex, and cannot be compared with any other magnetic application worldwide. Indeed, the whole magnetic system includes 1,234 fifteen meter long dipolar magnets, weighting 34 ton each, and 392 main quadrupolar magnets, all been made with superconducting wires, for a total of 7,000 km of multi-strand cables cooled with 94 tons of liquid helium in order to generate a 12,000 A steady current. Current magnets installed at the LHC, which led recently to the experimental validation of the Higgs boson, are based on NbTi technology but this material reaches its limits at 10 T, the critical magnetic field beyond which the material looses its superconducting properties. As access to smaller components of matter will require higher energy, the next generation of magnets will require materials that could keep superconductivity above these critical fields to allow for a higher current intensity being provided for higher magnetic fields (Devred et al., 2005). Until now, the best candidate remains Nb_3Sn, an intermetallic compound of the A15 family, which keeps superconducting properties at 12-15 T (Matthias et al., 1954; Kunzler, 1961; Matthias et al., 1963; Echarri and Spadoni, 1971; Dew-Hughes, 1975; Ashkin and Gavaler, 1978; Van Kessel et al., 1978; Hulm and Matthias, 1980; Muller, 1980; Godeke, 2006; Boutboul et al., 2008). Unlike other candidates like high Tc superconducting ceramics or MgB_2, the technology for the manufacturing of Nb_3Sn strands is well developed and hundred of meters can be manufactured at the industrial level. Nevertheless, the use of these materials for the design of large dipoles and quadrupoles elements is still facing numerous technological

challenges (Hafalia et al., 2005; Caspi et al., 2007; Felice et al., 2007; Ferracin et al., 2007; Nobrega et al., 2007; Miyazaki et al., 2008; Nobrega et al., 2008; Breschi et al., 2009).

1.2. Preparation and properties of Nb_3Sn

Nb_3Sn strands are prepared with two methods that both involve a direct reaction between niobium and tin at 600-700°C under neutral atmosphere for several days. In the Powder in Tube (PIT) route (Zlobin et al., 2005), the strand before reaction, is made of Nb-X tubes (X: Ti or Ta) filled with a mixture of Nb and Sn powders, embedded in a high quality copper matrix. After reaction, the tubes are laminated into wires. In the Internal Tin Diffusion (ITD), the strand consists of Nb-X filaments embedded into a mixed Cu and Sn matrix, surrounded by a Nb-X barrier which separates the multi-filamentary zones from a stabilizing, high quality Cu matrix. Upon heating, tin diffuses through the copper matrix up to the niobium wires where it reacts, giving a block that is further laminated into wires.

1.3. Challenges for using Nb_3Sn in magnetic reels

The design of all magnets requires very specific dimensional criteria, to fulfill strict parameters for the magnetic field geometry, which implies the bending of Nb_3Sn strands with a high curvature radius. Unfortunately, as Nb_3Sn is an intermetallic compound that becomes brittle upon reaction, this material can hardly been engineered once reacted, because any strain will create defects and crystalline dislocations that hamper dramatically the superconducting properties. Therefore, the sheath must be initially wound around the cable, this cable been further shaped and bent to achieve the magnet geometry before the thermal treatment that will synthesize the Nb_3Sn phase. This method named "wind & react" (Devred, 2002), prevents obviously from using any organic sheath or any material containing organic components, because the thermal treatment under neutral atmosphere would leave behind carbon residues that

would hamper electrical insulation. Moreover, the sheath must be flexible enough to allow winding, without cracks, but it must respect also excellent dimension constraints, and exhibit high mechanical strength to resist magnetic strains that will be generated under current.

As the magnet scale, forces and manufacturing route present real challenges for the conductor insulation technology, one method relevant to the current technology, has been explored until now. This method is based on the post-impregnation with resin of a glass fiber matrix. If it allows one to use current organic materials, its application remains confined to small demonstrators and it could not be applied for large scale manufacturing (Canfer et al., 2008). Hence, the real challenge was to develop an organic-free solution, based on ceramic components that could fulfill the complete and drastic bill of specifications.

The present report describes a method to manufacture a ceramic insulating sheath with processes that could be easily scaled-up, leading to an organic-free ceramic ribbon that can be stored before further use as an insulating sheath of Nb_3Sn wires, or for other applications. This process associates a glass fiber ribbon that provides a constant thickness, with the impregnation of a dispersion of ceramic precursors. This dispersion must fulfill different criteria: (i) being stable with time, (ii) being rather fluid during the impregnation step, (iii) becoming rapidly rigid to prevent any drip after application, (iv) being a good electrical insulator after the thermal process.

The present insulating sheath fulfills the required criteria: it resists well to the synthesis of Nb_3Sn (300 hours at a temperature range between 600 and 750°C) that is actually used to achieve the formation of this insulating sheath, it presents a well-defined thickness (around 130 μm) under a 80 MPa pressure, and results of electrical and magnetic tests, validated by the assembling of a demonstration reel that could conduct a 194 A current under a 11 T magnetic

field, in the superconducting state of Nb_3Sn, confirm that the ceramic sheath is not detrimental to the superconducting properties.

2. Experiments

2.1. Materials

An initial set of ceramic precursors was tested to check their adequacy with the expected properties, that is, exhibiting good film properties in the crude state, and providing a good structural evolution upon sintering at low temperature ($\approx 650°C$) under neutral atmosphere, a major challenge for ceramics that are usually sintered in air at higher temperatures. Different raw materials were tested, all based on clay minerals (BIP™ or (BIP Kaol) CGU™ (CGU Kaol) kaolinite, Arvel™ (Arvel Mt) or Expans™ (Expans Mt) Montmorillonite). Compared with synthetic clays, it is well known that properties of natural minerals change with time and from a batch to another one. Therefore, the whole procedure must allow one to adapt the final composition in agreement with a required property. The rheological behavior of the aqueous dispersion was selected as a reference for the further selection of components proportions. As the thermal treatment for the synthesis of Nb_3Sn occurs at a rather moderate temperature, compared with usual ceramic processes, the structuring agent (the clay mineral) had to be combined with a low temperature frit (2495F from Johnson & Mattey: melting temperature at 538°C). The absence of Boron in the additive, an element that can diffuse under irradiation, was checked before use. The final ceramic sheath was prepared by the impregnation of a 15 mm large (0.12 mm thickness) weaved glass ribbon (Type S2 from Hiltex Technische Weefsels Co.). As these glass fibers are initially coated by an organic layer, this latter was removed before use with a 10 hour thermal treatment at 350°C in air. The fibers became extremely brittle after

treatment, but their recovered their initial mechanical properties after a 48 hour curing at room temperature under a moderate moisture (Devred, 2002). Nb_3Sn/Cu wires were kindly provided by Alsthom Cie. These wires have an overall section of 0.535 mm^2, with a Nb_3Sn/Cu ratio of 1, and a Nb_3Sn section of 0.267 mm^2.

2.2. Preparation

2.2.1. Preparation of the ceramic dispersions

A typical preparation of the aqueous dispersion was carried out according to the following procedure: (i) 160 g of the sintering frit was poured under strong mechanical stirring into 160 mL of deionized water; (ii) the solution was defragmented for a total active time of 10 minutes under ultrasounds - 2 sec. pulses - with a sonication gun (650 W Vibracell with a 15 mm diameter sonication probe); (iii) the solution was left for 4 hours under stirring to allow the pH to stabilize (final pH $\approx$ 11); (iv) 80 g of clay mineral was slowly added under strong mechanical stirring to avoid the formation of aggregates; (v) the solution was left under sonication for 10 min - same procedure as for (ii) - and stored; (vi) before use, the solution was stirred for 12 hours on a roller stirrer, after the addition of 20 balls of vitreous china (10 mm diameter) for 12 hours. In the following, the proportions of components were adjusted according to the experimental points in the phase diagrams.

2.2.2. Design of the impregnation bench

A specific impregnation bench was designed and assembled to allow the impregnation of long length of glass ribbons by the ceramic dispersion. A schematic and a photo of this apparatus bench are displayed in Figure S1 (in ESI), top and bottom, respectively. The different parts of this system include: (1) an initial roll of the glass ribbon (thermally treated beforehand to remove organics) that can deliver the ribbon with a constant tension through an electromagnetic

brake (MAYR, France); (2) a 500 mL beaker of the ceramic dispersion in which the glass ribbon is firstly dipped, then pressed between rolls in order to achieve a good impregnation of the ceramic dispersion; (3) a magnetic stirring to keep the ceramic solution fluid (the specific thixotropic behavior of the ceramic dispersion allows it to gel as soon as the ribbon is pulled out from the beaker); (4) a dryer made of a tube (53 mm diam., 320 cm length) equipped with a seven meter heating wire rolled over a 2.66 m length, heated at 110°C; (5) an in-line thickness control provided by a laser telemeter (Jeanbrun Automation); (6) a winding system with varying speed set at 30 cm.min^{-1} that allowed us to obtain at the end a full roll of the dried glass ribbon impregnated with the ceramic mixture (clay + frit). A thirty-meter reel of ceramic ribbon was successfully prepared (Figure S2), the roll being stored before further use. This method allowed us to totally differentiate the preparation of the ceramic ribbon from the winding operation, which provides much more flexibility in the future scale-up process.

2.3. Methods

2.3.1. Rheology

Rheology measurements of the different ceramic dispersions were carried out at 20°C, with a Thermo Haake Rotovisco 1 rheometer with a cylinder/cylinder geometry. Measurements were recorded with a spinning speed Gp varying from 0 to 800 cm.s^{-1} and back. The evolution of the strain τ versus Gp was measured from which viscosity $\eta = d(\tau)/d(Gp)$ was deduced. For Newtonian fluids, η is constant and the evolution of τ with Gp is linear, but non-linear evolutions reveal a non-Newtonian behavior.

2.3.2. Mixture Design

The experimental points studied were determined by using a mixture design analysis, the response being the viscosity of the different dispersions. Results were analyzed with

STATISTICA™ (StatSoft Co). From the experimental values, the whole mapping of viscosity was calculated as a quadratic response:

$$Y = (B_1 \times X_1) + (B_2 \times X_2) + (B_3 \times X_3) + (B_{12} \times X_1 \times X_2) + (B_{13} \times X_1 \times X_3) + (B_{23} \times X_2 \times X_3) \quad (1)$$

With Y being the parameter, that is, the viscosity, X_i the respective mass concentrations within the restricted phase diagram, B_i and B_{ij}, the coefficients calculated from the experimental values from the set of measurements. For non-Newtonian fluids, Y was chosen as the mean viscosity deduced from the average of the curve measured during the decreasing spinning speed, between 600 and 200 s^{-1}, since the thixotropic behavior of the ceramic dispersions allowed for a rather Newtonian behavior upon spinning speed reduction.

2.3.3. Thermal treatment

After selection of the ceramic mixture optimized for a given rheological behavior, sintering tests of ceramic ribbons were carried out on stacks of 30 ribbons (5 cm length) confined in a stainless steel mold designed for the parallel treatment of 10 stacks. Different thermal treatments under neutral atmosphere were ran, with temperatures of 660°C, 720°C and 750°C, respectively, and a sintering time of 50 hours. The volumic mass was measured with an helium picnometer.

2.3.4. Mechanical resistance under compression

The mechanical resistance of stacks of ribbon under compressive loading was characterized with an INSTRON electromechanical platform that can apply a 150 kN load, with a 0.2 mm.min^{-1} translation speed of the loading head. An uniaxial load of 96 kN over the sample surface (120 mm^2) was applied, corresponding to a pressure of 80 MPa.

2.3.5. Residual Resistivity Ratio (RRR)

Residual Resistivity Ratio (RRR) measurements were carried out to verify that the property of the copper matrix of the Rutherford cables, remains unchanged after ceramic coating. In a typical RRR measurement, a current ($I = 1$ A) is flowing through a wire inserted into a four contact measurement set-up (two for current application, two for the potential measurement). Two measures V' and V" were recorded with the current flowing both ways, and subtraction of the two values allowed us to determine the thermoelectrical tension e, and give access to the intrinsic resistance:

$V' = RI + e$ & $V'' = -RI + e$ (2)

$R = (V' - V'')/I = (V' - V'')$ (with $I = 1$ A)   (3)

The RRR value of a superconductor is defined as the ratio of resistivity at 273K and at the transition temperature, that is, 18.3 K for Nb_3Sn:

$RRR = (\rho_{273K}/\rho_{18.3K}) = (R_{273K} \times L)/(R_{18.3K} \times L) = R_{273K}/R_{18.3K}$ (4)

2.3.6. Critical Current

The critical current measurements were carried out with a standard VAMAS ("Versailles Project on Advanced Materials And Standard") module, designed to allow for microvolt potential measurements (see Figure S3) (Gould and Wada, 1995). An Nb_3Sn wire was wound around a reel with specific dimensions, and electrical potential was recorded over a short length, with two measurement positions (half-turn = 45 mm (V2), whole turn = 90 mm (V1)). The influence of the ceramic preparation was tested, as for the RRR measurements, by coating the VAMAS reel with the wet ceramic dispersion, in order to increase interactions with the superconducting wires. The current at low temperature and high magnetic field was recorded on the CétacéS station ("Cryostat d'Essai Température Ajustable Champ Elevé Saclay", CEA Saclay) (Figure S4), which allows for measurements with a maximum magnetic field of 17 T, and a temperature range

varying from 40 to 1.8 K. The critical current I_c was obtained by measuring the electrical potential over a short wire at 4.2K, in the superconducting state ($T_{trans.}(Nb_3Sn)$=18.3 K), as a function of the current intensity. As the intensity increases, the potential initially equal to zero, will increase slightly as a result of the first de-anchoring of current flow tubes - a reversible state -, followed by a catastrophic de-anchoring of all current flow tubes and the irreversible transition toward the resistive state. The transition (or quenching) current I_q corresponds to this irreversible transition, but the occurrence of the intermediate reversible state does not allow to define precisely the value of the critical current I_c, which remains below I_q. Therefore, a standard environment defined with the apparent electrical field E_{sc} and the apparent electrical resistivity ρ_{sc} is defined as:

$$E_{sc} = V_w/L_w \qquad (5)$$

$$\rho_{sc} = (1/1+\lambda_w) \text{ x } E_{sc}(S_w/I_w) = (1/1+\lambda_w) \text{ x } (V_w/L_w) \text{ x } (S_w/I_w) \qquad (6)$$

With L_w the wire length, S_w its section, λ_w the copper over non-copper ratio, and V_w the potential. The value of I_c is defined for E_{sc} = 0.1 µV.cm-1, or ρ_{sc} = 10^{-14} Ωm, and the critical current density J_c (A.mm^{-2}) can be deduced from the measurement of I_c, according to:

$$J_c = I_c \text{ x } [(1+\lambda_w)/S_w] \qquad (7)$$

J_c was deduced from the measurements of critical current I_c, deduced from a series of analyses of the V(I) curves measured at 4.3 K, with the magnetic field varying from 5 to 15T. The measurement of the critical current was completed by a characterization of the first derivative of the potential- intensity curve close to the transition. This function is described as:

$$V_w/V_c = (I_w/I_c)^N \qquad (8)$$

with $V_c = E_c \text{ x } L_w$ being the potential applying on the sample for the value of the critical field E_c, and N being a parameter described as the index of the resistive transition, or "N-value". It

results that N can be easily determined by plotting $Ln(V_w)$ *vs* $Ln(I_w)$. The value of N allowed us to identify the origin of the transition, described by the critical current, which can be either due to intrinsic parameters (material relevant), and/or to extrinsic degradations (engineering and processing relevant) (Warnes and Larbalestier, 1986). It is usually assumed that the highest the derivative (the more abrupt the transition), that is, the highest the N-value, the better the superconductor.

For each value of magnetic field, the V(I) curves were recorded with a 3 A.s⁻¹ ramp until a potential three times larger than E_{sc} was observed. Each curve allowed us to determine the values of N and I_c, from which J_c was calculated according to eq.(7). Both I_c and J_c are strongly dependent on both temperature and magnetic induction, and it was demonstrated that the transition intensity I_q can be deduced from these values (Devred et al., 1992). J_c depends not only on the magnetic field and temperature, but also on the wire strain (Summers et al., 1991).

2.4. Demonstrator for magnetic tests

2.4.1. Assembly

Titanium VAMAS geometry was used to assemble a testing reel in order to probe how the ceramic insulation can stand very high external magnetic fields and resist to magnetically induced Lorentz forces created by the superconducting strands. The whole testing reel had to respect very strict dimensions (50 mm length, 40 mm external diameter, 18 mm internal diameter) in order to fit within the CétacéS measurement chamber. Tests were carried out with the current flowing both directions in order to validate not only the geometrical stability of the reel under centripetal Lorentz forces - a usual test -, but also the mechanical resistance of the ceramic coating under the strong centrifugal Lorentz forces created by the current flowing through the superconductor (Figure SI.5).

The demonstrator was built according to the method displayed in Figure S6: the reeling process led to a testing reel made of 270 spires distributed over 9 layers sandwiched with the ceramic sheath. The reel was placed in the CétacéS platform at the temperature of liquid helium, under an external magnetic field $B_{CétacéS}$ of 11 T, with a current varying from 0 to 194 A applied to the demonstrator reel, generating an induced magnetic field B_{Reel}.

All tests were ran at current values limited at 85% of the critical current of the superconductor, to be sure that any degradation in properties would result only from the ceramic insulation. The first series of tests (centripetal forces) was carried out according to standard procedures with a current noted +I. With this test, the magnetic field B_{Reel} induced inside the reel, opposes to the external magnetic field $B_{CétacéS}$ created by the CétacéS platform, and the maximum magnetic field applied to the reel is located outside the reel, where $B_{Reel} = 0$. It results that for the (+I) configuration, $B_{max} = B_{CétacéS}$. For the (+I) test, as the induced Lorentz forces are centripetal, the mechanical resistance of the VAMAS core titanium chuck limits compressive strains. The second series of tests was carried out with the reversed current (noted -I) leading to centrifugal Lorentz forces. As B_{Reel} and $B_{CétacéS}$ are parallel, the resulting $B_{max} = B_{Reel} + B_{CétacéS}$ are located inside the reel, and the resulting centrifugal forces create dilatation strains that apply only onto the ceramic insulation.

2.4.2. Measure of the critical current

The ability to build superconducting Nb_3Sn magnets with a ceramic insulation sheath was finally validated by the determination of the critical current I_c reached by this demonstrator. This critical current I_c is usually determined by the superconducting-to-resistive transition (quenching), related with the actual magnetic field B_{max}, which will depend on the (+I) or (-I) configuration (Figure S5). In standardized measurements, I_c is assigned to the current required to observe a 0.1

μV.cm^{-1} variation in potential. However, with the 20 m conductor length used for this test, running tests up to a total variation $\Delta U = 200 \; \mu$V, could irreversibly damage the strand - and the experimental chamber -, with a Joule effect resulting from brutal quenching that could vaporize liquid helium.   Therefore, an experimental critical current I'_c was defined when the electric potential was observed to vary out from its steady value. It results that the true critical current I_c should be higher than the experimental value I'_c.

3. Results and Discussion

3.1. Rheological measurements

3.1.1. Results for BIP Kaol, CGU Kaol and Arvel Mt

The final composition was selected out of four materials: BIP Kaol and CGU Kaol, Arvel Mt and Expans Mt. For all, preliminary tests allowed us to determine the best concentration range within a (water:clay: frit) ternary diagram, from which the mixture design analysis was carried out. The initial domain was selected based on visual inspection of dispersions, which had to be homogeneous and not too dilute.   The two kaolinite-based dispersions exhibit a Newtonian flow, and they precipitate over time (Figure S7 & S8). For both, the map response of viscosity illustrates that the viscosity increases directly with the increasing amount of the mineral phase.

The dispersion made with Arvel Mt (Figure S9), differs largely from the two previous ones. Rheological tests show that the samples with the higher concentration in clay present large hystereses between the increment and decrement of spinning speed Gp, and the curve shape reveals a rheofluidifying behavior. These hystereses are particularly large for samples B, C and E, which correspond to samples with the highest content in solid phase (clay + frit), as illustrated in the response map, with the highest viscosity along the frit-Arvel Mt axis.

Compared with BIP Kaol and CGU Kaol, this material provides the expected thixotropic property, but it seems difficult to easily adjust it. The rheological curves illustrate also a sharp transition between the rheofluidifying and the Newtonian behaviors, which should also contribute to narrow the composition range where the expected properties can be encountered.

3.1.2. Results for Expans Mt

Unlike Arvel Mt, preliminary tests with Expans Mt in the same concentration range as other samples, revealed a very strong thixotropic behavior. The domain of study of the ternary phase diagram was modified accordingly, in order to obtain samples that do not present a too high viscosity. As illustrated in Figure 1 (see Table SI for sample composition), the new domain of composition was based on a constrained mixture study with four points (A, B, C, D) at the corner plus five additional points (E to I) within this area.
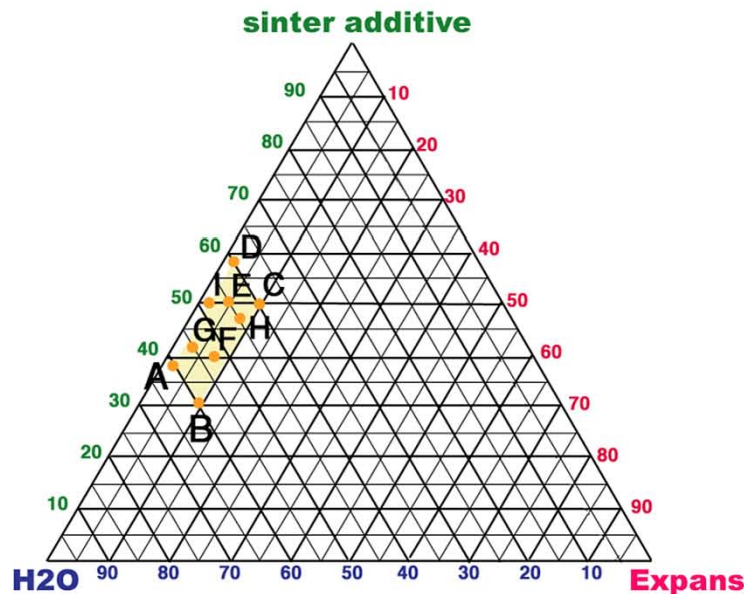
Figure 1. Phase diagram and sample composition mapping for the mixture of Expans Mt clay and frit in water.

Even at these low concentrations, the aqueous dispersions are quite homogeneous and stable, as illustrated in Figure 2, with samples prepared for the mixture design study, and left at rest for 12 hours. For most of the samples (Figure 2.a), the preparation is stable, even though a small phase separation can be observed for some (sample A). With sample D that contains the same amount of Expans Mt as A, but a lower amount of water, this phase separation does not exist. All dispersions have a strong thixotropic behavior and some display a very impressive gelling as soon as the stirring is stopped (Figure 2.b), as these samples are only made with a rather small amount of clay mineral or sintering frit, and no organic additive.

Figure 2. (a) dispersions of clays after 12 hours at rest and (b) illustration of the thixotropic behavior of some samples (sample D).

Unlike the rheological curve obtained with Arvel Mt that could differ drastically from one sample to another (Figure S9.c&d), the rheology curves obtained with Expans Mt are quite

uniform, with a steady transition from Newtonian to rheofluidifying curves and smaller hystereses (Figure 3).
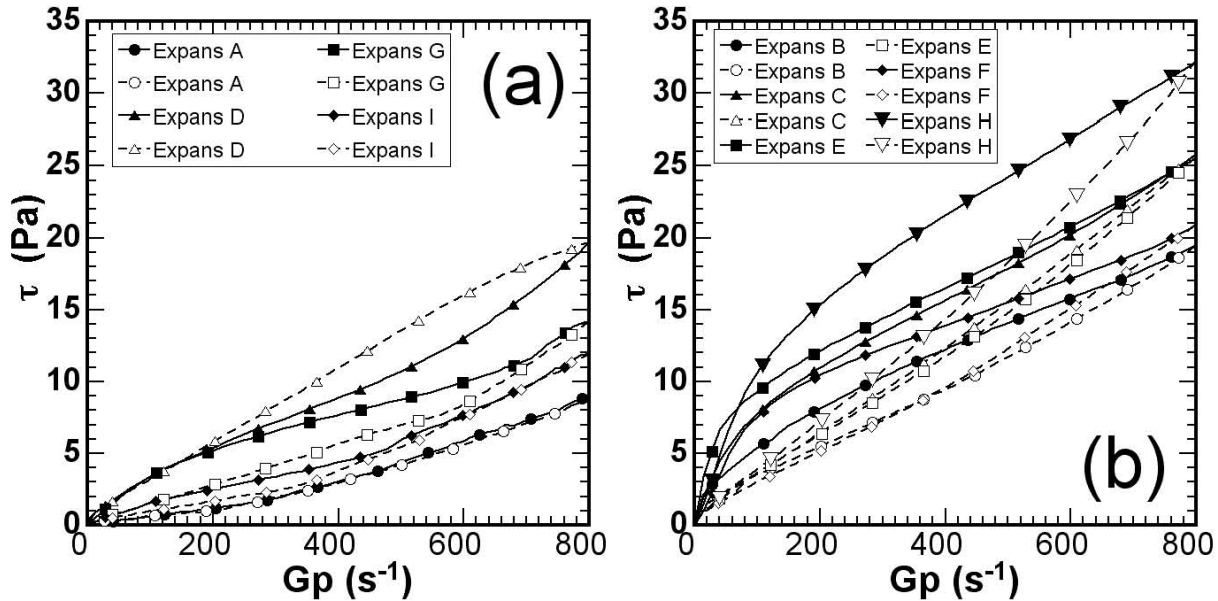
Figure 3: Rheology curves for samples prepared with Montmorillonite Expans Mt: (a): samples with a Newtonian behavior; (b) samples with a thixotropic behavior (lines: increasing speed; dashs: decreasing speed); for compositions, see Table I.

Samples with the lowest amount of Expans Mt (A, G, I) display a rather Newtonian behavior, and compositions with the highest load in mineral (B, C, E, F, H) a thixotropic one. This thixotropic property is confirmed by the decreasing spinning speed curve - recorded just after the increasing speed curve - that follows a Newtonian behavior, as a proof that the initial viscous state is recovered only after a given time. Interestingly, sample D presents an intermediary stage as it contains a low amount of Expans Mt but a high load in frit.

The definition of viscosity applies only for a pure Newtonian fluid where both the curves $\tau=f(Gp)$ with increasing and decreasing spinning speeds overlap. With this limit in mind, the decreasing spinning curve was used anyway to calculate the intrinsic viscosity of the ceramic

dispersions free from thixotropic contributions. These values were used in the response map displayed in Figure 4.a. They increase along a specific axis from the water-frit basis (with 0% clay) to the Expans Mt apex, with a sharp increase of viscosity as soon as the total mineral amount (clay + frit) has reached a few %. The thixotropic itself was quantified by the surface between the increasing and decreasing speed curves (Figure 4.b). The contribution to thixotropy of the ceramic dispersions is more continuous, but still, even a small amount of Expans Mt induces a thixotropic behavior, which is totally different from what observed with the other materials (BIP Kaol, CGU Kaol, Arvel Mt).
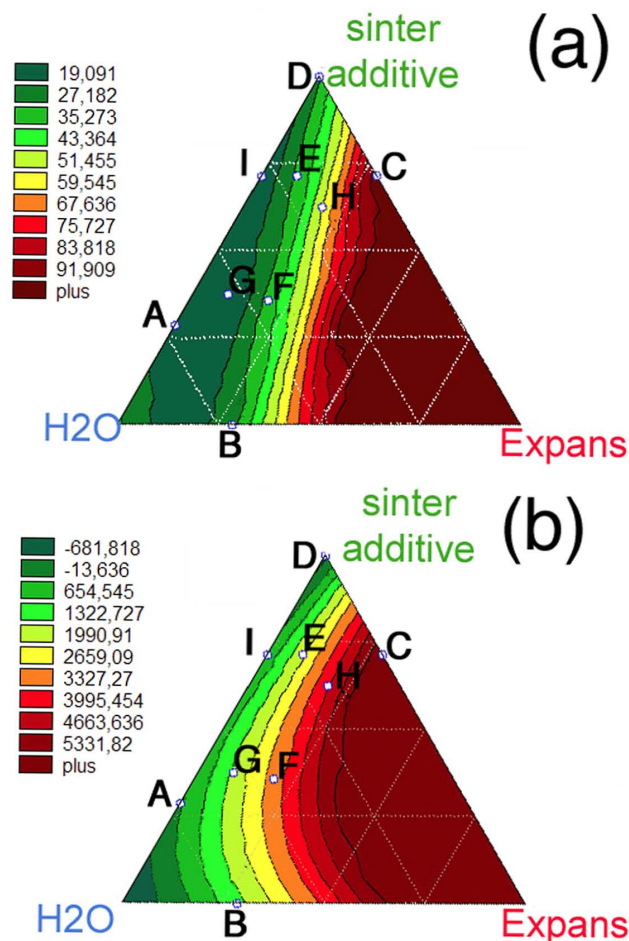
Figure 4. Evolution of (a) the viscosity (mPa.s^{-1}) and (b) the thixotropy for samples prepared with Expans Mt.

3.2. State and plasticity of impregnated glass ribbons

Beyond the properties of the ceramic dispersions themselves, the ability for these preparations to correctly fill and cover the glass ribbons, and keep a sufficient plasticity after drying, to allow for future winding, was tested. Therefore, impregnation tests of glass ribbons were carried out by a manual impregnation of ribbons with a spatula, drying at room temperature. Their flexibility was quantified by bending the ribbon around a 5 mm diameter iron-steel cylinder.
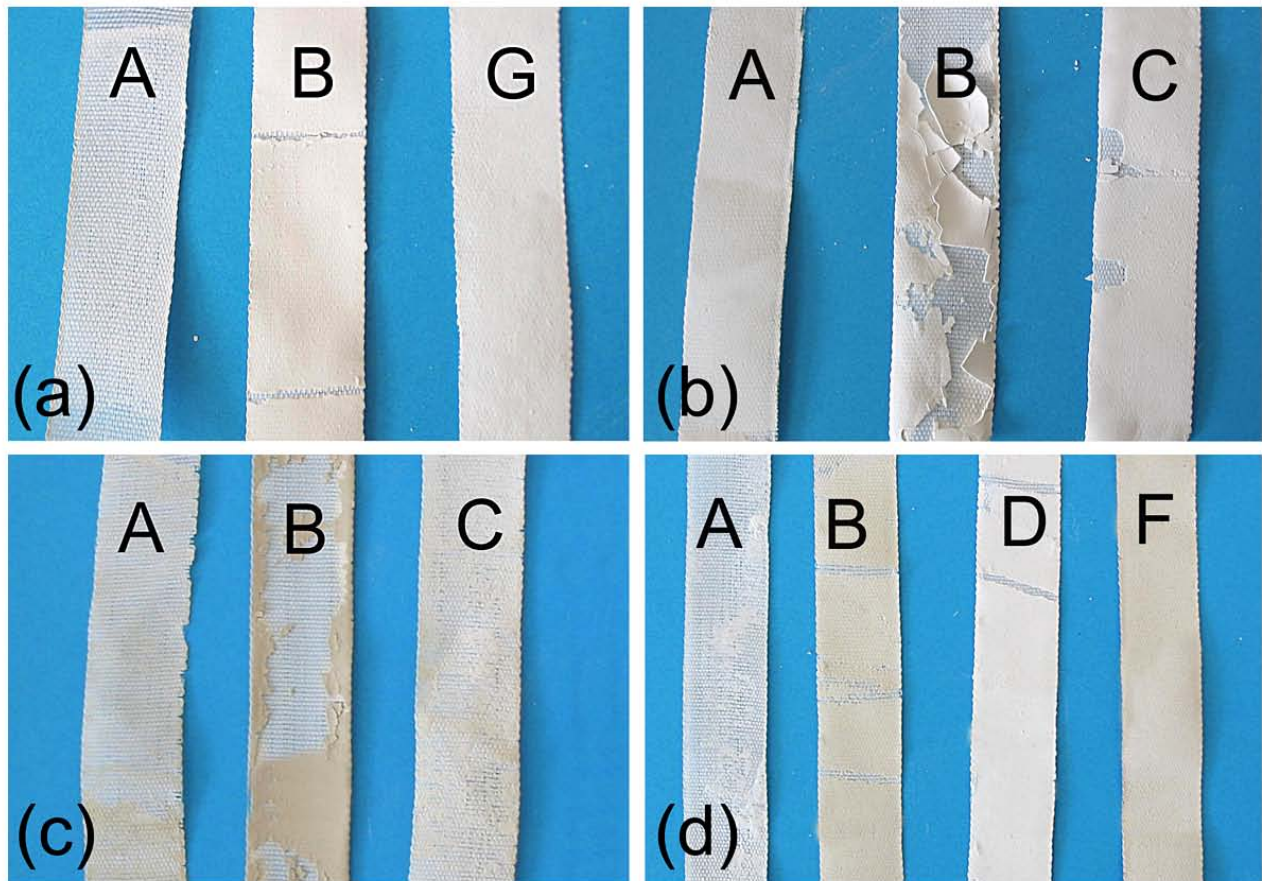
Figure 5: Glass ribbons impregnated with different ceramic compositions based on (a) BIP Kaol BIP, (b) CGU Kaol, (c) Arvel Mt and (d) Expans Mt. Visual inspection after ribbons bending.

The four minerals present different results as displayed in Figure 5. With ceramic samples that were not viscous enough, the final ceramic film is too thin and only a part of the ribbon is actually filled with the ceramic mixture after drying (Figure 5. (a,c,d), sample A). On the other side, a too viscous solution leads to a thick and rigid layer that breaks upon bending (Figure 5.b -sample B- or 5.c -sample C-). It was deduced from these tests that the best candidate must combine a good thixotropic behavior to give good quality films, with a concentration is mineral components that is high enough to fully fill and cover the glass ribbon. In addition, the intrinsic properties of the ceramic layers must allow a good plasticity, which is the result of clay addition. For this test, the best compromise was still obtained with Expans Mt (Figure 5.d -samples D & F-) that allowed the formation of continuous and smooth films that can stand the bending test.

3.3. Choice of the clay, and composition

Both the rheological and glass ribbon impregnation tests, led to conclude that Expans Mt was the best candidate, with the following composition (in mass%): water: 50; frit: 40; Expans Mt: 10 (viscosity ~ 40 mPa.s). This composition is a good balance between thixotropy, easy flow under small shearing, rapid freezing upon shearing stop, and excellent stability of the aqueous dispersion over time. Nevertheless, it is well known that natural clays have properties that can vary with time, or from one batch to the other. It would result that the same composition with a different batch, could lead to different results, which was observed, as a new batch of Expans Mt was used. From comparison of the rheological curve obtained with the old batch (Figure 6: old clay- old formulation), with the new batch and same composition (Figure 6: New clay - old formulation), it appeared clearly that the optimum composition deduced from the initial batch could not be transferred to the new one. Hence, the initial rheological curve was

taken as the reference, instead of the composition, and the composition with the new batch was adapted in order to recover the same rheology. This is illustrated with a sample prepared with a composition adjusted accordingly (Figure 6: New clay - new formulation): water = 42.5 mass%; frit = 46 mass%; Expans Mt™ = 11.5 mass% (viscosity ~ 45 mPa.s). This composition was used for the rest of the study.
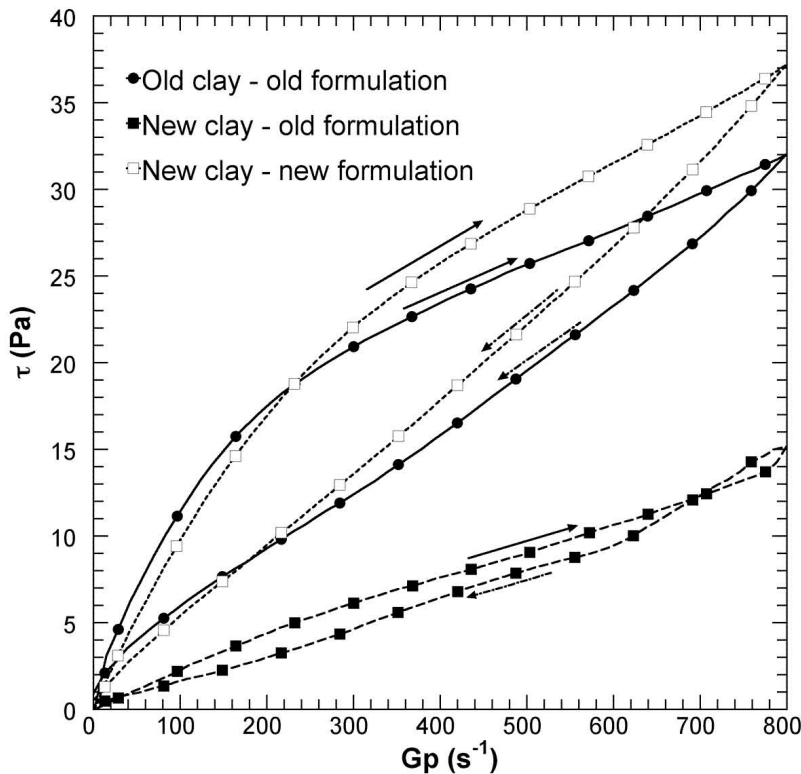
Figure 6: Rheology curves for the initial stock of clay (Expans Mt) with the formulation deduced from sampling study, for the new stock of clay with the same formulation as for the previous one, and for the new stock of clay with a formulation adapted to fit with the initial rheology curve.

3.5. Thickness of the ceramic ribbons in the crude state

Once the optimum composition had been chosen, the continuous impregnation and drying of a complete ribbon (30 m long) was proceeded with the impregnation bench described

hereinbefore (Figure S1). This method gave a crude ceramic ribbon, as illustrated in Figure S2, which was used for the rest of the study. The average thickness of this crude ribbon, measured with a Palmer, at different locations of the ribbon, was equal in average to 200 μm. The thickness variation of the 30 meter dried ceramic ribbon was evaluated with the in-line controller, and an average variation of $\pm$ 25 μm was observed (Figure S10). The first three meters exhibit a random variation in thickness, due to initial fluctuations, but this thickness becomes rapidly rather constant, with some random variations to 300 μm due to remaining powder aggregates. The 200 μm thickness seems still too high compared with the expected final value (120 μm) required by the 120 μm is the expected thickness after sintering and under magnetic-induced mechanical compression. The ribbon thickness measured with a stack of 20 crude ceramic ribbons (4 mm total thickness) under an 80 MPa compression stress (Figure S11), showed that the initial 4 mm thickness decreased to 3.28 mm (18%), which corresponds to a thickness of 164 μm for a single ribbon.

3.6. Thermal treatment of the ceramic sheath

3.6.1. Sintering

The evolution of the ceramic ribbons was followed as a function of the thermal treatment required for the reaction of Nb_3Sn. Achieving a good cohesion of the ceramic body is actually a challenge because the parameters required for the synthesis of Nb_3Sn (T < 800°C,, inert atmosphere, several days of reaction time) are at the opposite of what is usually required for a good sintering (high temperature, fast process, oxygenated environment). A stack of 30 impregnated ribbons was confined in a copper mold and exposed to a temperature of 660°C, 720°C or 750°C for 50 hours under neutral (Ar) atmosphere. The volumetric mass of the stack was measured after the thermal treatment (Figure 7).
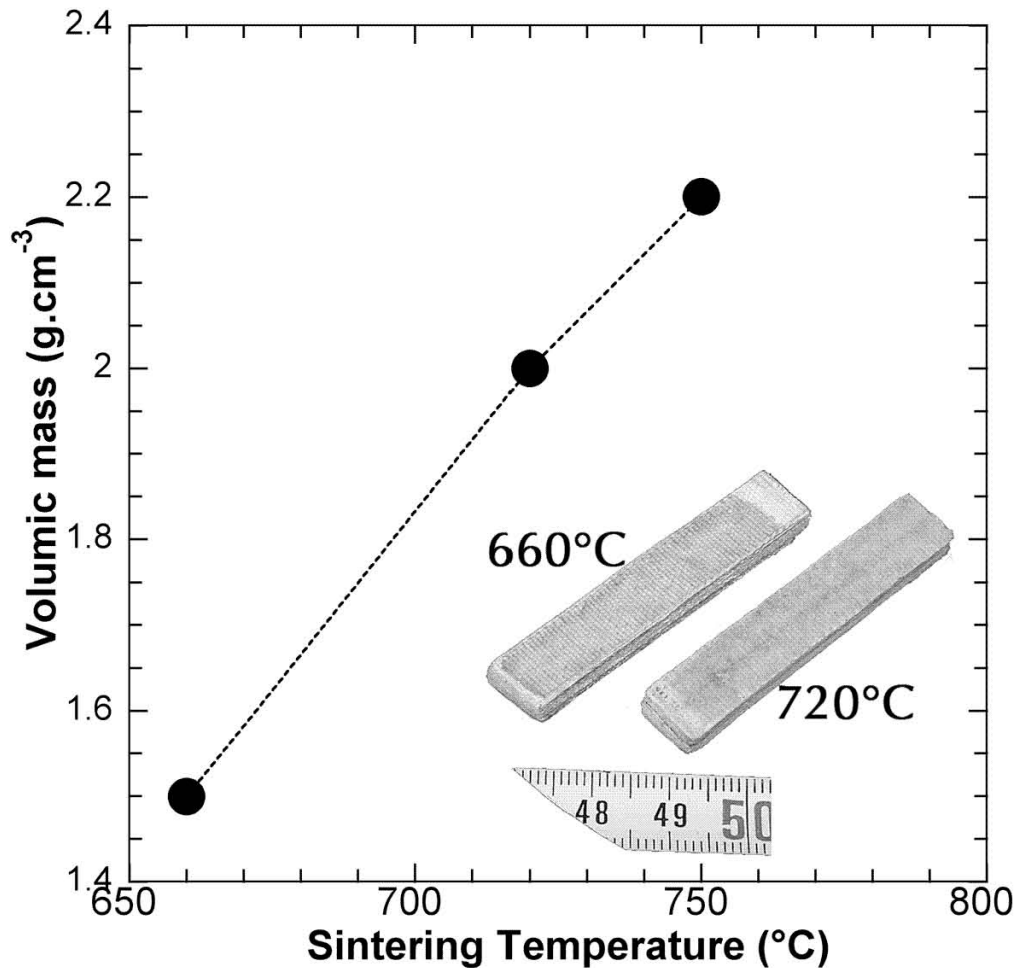
Figure 7: Evolution of the Volumic Mass of ceramic ribbons as a function of the sintering temperature. inset: visual observation of stacks of 30 ceramic ribbons sintered at 660 and 720°C for 50 hours, under neutral atmosphere.

A first visual inspection (Figure 7.inset) of the thirty-ribbon stack after sintering, demonstrates that a good cohesion was obtained between the ceramic ribbons. The stack submitted to the highest temperature exhibits a glassy-like structure and a higher shrinkage is observed (dimensions from 12 x 4.5 mm down to 11 x 3.5 mm). The evolution of the density as a function of the sintering temperature, as reported in Figure 7, shows that the full density of silica is reached at 750°C. SEM observations (Figure 8) illustrate more precisely the evolution

of the ceramic structure between 660 and 720°C. Important cracks and unreacted particles of the frit are observed after treatment at 660°C (Figure 8.a), and a lack of cohesion between the different ribbons is also observed (Figure 8.b). Rising the sintering temperature at 720°C helps to decrease drastically the density of surface cracks (Figure 8.c) along with a better inter-ribbon sintering (Figure 8.d).
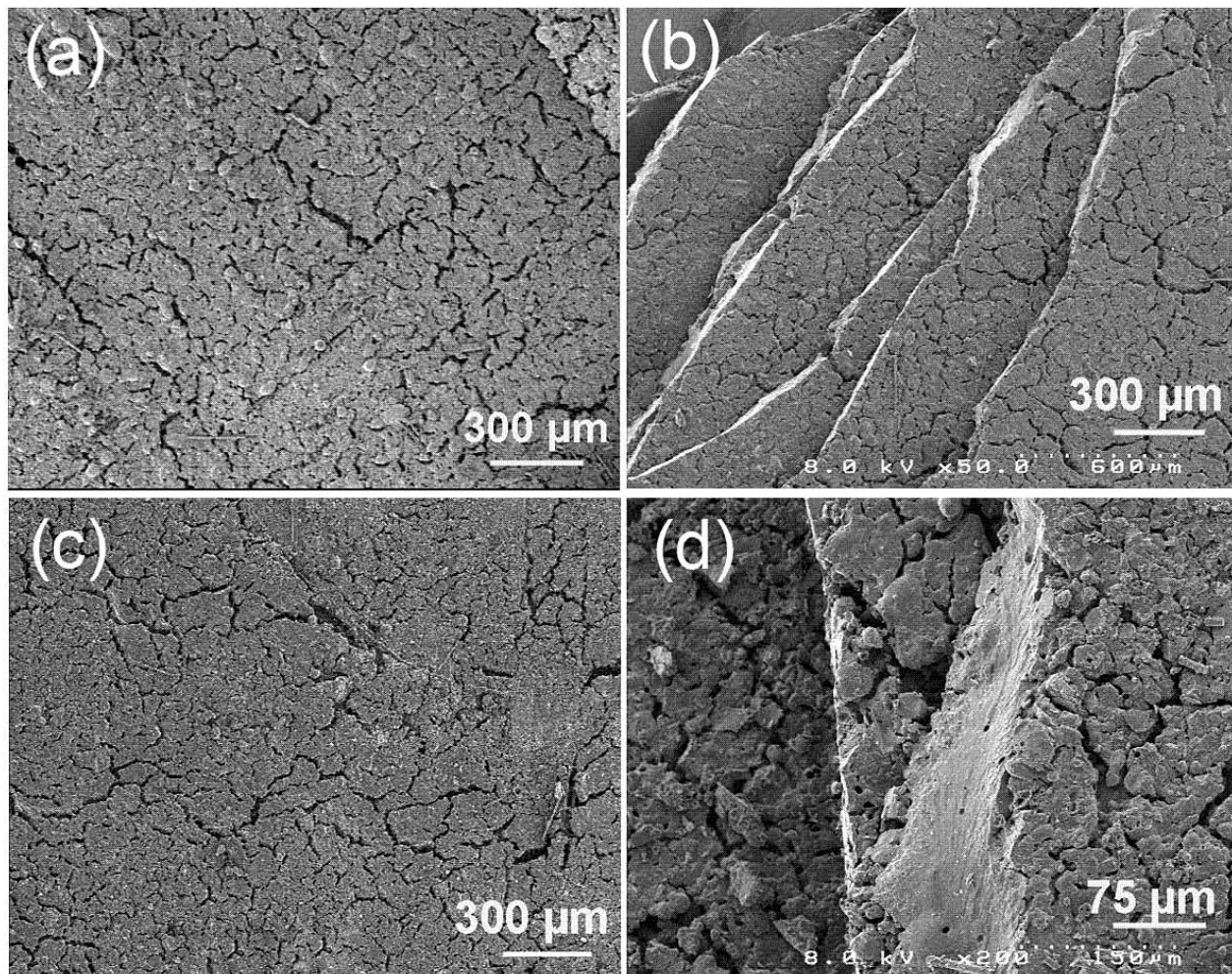
Figure 8: SEM observation of the stacked ribbons sintered at 660°C (a & b) and 720°C (c & d).

The sintering role of frit was confirmed by running dilatometer analysis with a temperature plateau set at 620°C (with sample J2, Table SII). The resulting curve (Figure S12)

shows an actual shrinkage resulting from sintering, this pellet starting sinter at the expected temperature, and sintering being complete after less than two hours. As the pellet was not confined, the foaming phenomenon, which had been observed with other samples (see below), was not noticed.

3.6.2. Ceramic foaming

The actual influence of the ceramic components was explored by varying the ratio of the sintering agent over (frit + Expans Mt) (Table SII). Based on previous results, sintering was performed at 660°C and 720°C with a thermal cycle similar to that applied to ribbon stacks. These experiments were carried out with pressed pellets confined between two copper plates to mimic the influence of confinement during the future sintering of ceramic ribbons. The different pellets before and after thermal treatment are displayed in Figure S13. Surprisingly, a foaming appeared, which increased with the increasing amount of frit, even though it contains no volatile compounds. However, the influence of the percentage of frit is clear, and the phenomenon increased with the sintering temperature, or frit increasing. Thermal analyses (TGA and DTA) revealed that the Expans Mt exhibits a large gaseous release from 100°C (Figure S14), which was identified by TGA-coupled mass spectrometry as H_2O and CO_2, CO_2 resulting from the clay decarbonation.

The combination of Expans Mt and frit leads to a coupled mechanism, similar to that observed in pumice stone formation. As clay dehydration and decarbonation occurs in a temperature range where a progressive melting of the frit turns it into a viscous material, gas bubbles are trapped within the melting glass, as confirmed by SEM (Figure S15), this mechanism being enhanced by the confinement provided by the copper mold and the thickness of the sample, and amplified by increasing both the frit percentage and temperature. Such a phenomenon was

not observed with the ceramic ribbons because their thickness allowed the gas to escape without being trapped. It results that an additional thermal pretreatment should be added to ensure the correct departure of all volatile compounds. However, a partial control of this foaming could be an interesting additional mechanism, as it would generate a porous framework within the ceramic insulation, which is suitable to conduct the cooling liquid helium directly to the surface of the superconducting strand. Such a close contact at the surface of the superconductor strand is a way to prevent any catastrophic magnet quenching by easily eliminating the extra heat that could be generated locally, before it extends over the whole structure.

3.6.3. Final structure

The ability of the ceramic ribbons to wrap correctly a rectangular Rutherford wire and to connect a stack of 10 with a good mechanical resistance was first tested. A ceramic sheath was created by wrapping the ribbon around Rutherford strands, without no overlap. A ten-stack of Rutherford wires was sandwiched within the two parts of a copper mold, then thermally treated under Argon at 660°C for 50 hours. Figure 9 displays the first coherent ten-stack obtained with an organic-free ceramic insulating sheath.
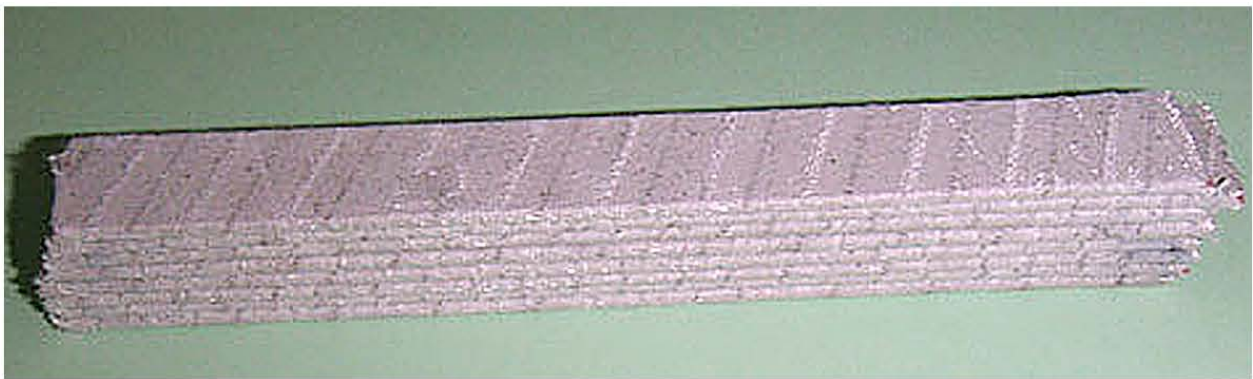
Figure 9: Ten-stack of Rutherford wires wrapped with ceramic sheath, after thermal treatment.

3.7. Electrical properties of superconducting strands

3.7.1. RRR measurements

The influence of the ceramic coating on the electrical properties of the copper matrix above and before the superconducting transition of Nb_3Sn (T_{trans} = 18.3 K), was studied by comparing two single strand Nb_3Sn/Cu wires, one uncoated, and one coated with the ceramic dispersion by dipping and drying (Figure S16). At room temperature, the electric resistance R_{273K} of the uncoated and coated wire, are equal to 6,547 $\mu\Omega$, and 6,352 $\mu\Omega$, respectively. The evolution of the electrical conductivity between 30 and 4 K is reported in Figure 10 for both samples. For $T > T_{trans}$, the evolution of the electrical resistance as a function of temperature, follows a T^5 law, a conduction law expected for a metal, because current lines flow through the less resistive part, that is, copper. Below T_{trans}, the electrical resistance comes down to zero. The electrical resistance $R_{18.3K}$ at T_{trans}., is equal to 19.9 $\mu\Omega$ and 21.9 $\mu\Omega$ for the uncoated and the coated wire, respectively. The RRR factor, as defined in eq.(4), drops from 329 for the uncoated wire, down to 290 for the coated wire, which is a value still by far above the minimum value accepted for large magnets (RRR > 100). Copper used in these wires is an ultra high purity metal and any minor pollution will affect its electrical conduction. As mentioned before, the ceramic dispersion has a basic pH (pH 11), which can induce the formation of a superficial layer of copper carbonate and/or oxide during the dipping step. At these levels of electrical conduction and sensitivity of measurements, even this superficial layer is detected by a slight reduction in conductivity. In the final process, dry ribbons instead of liquid dispersions are used, which should reduce this effect.
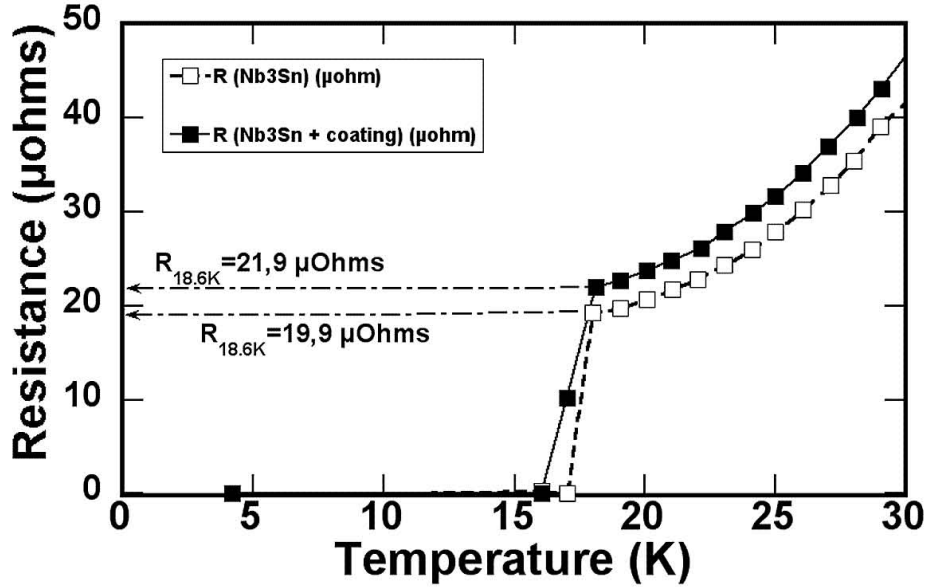
Figure 10. Evolution of the electrical resistance for Nb₃Sn/Cu wires without (white square) or with (black square) a ceramic coating.

3.7.2. Critical current

Superconducting properties of the Nb₃Sn material, once wrapped with the ceramic sheath, were checked by measuring the critical current of VAMAS reels (Figure S3) prepared with and without applying a ceramic coating. The evolution of the potential as a function of the increasing applied intensity, at 4.2 K, under a 10 T magnetic field (Figure S17) allowed us to determine the critical current I_c, with respect to the apparent electrical field $E_{sc} = 0.1 \ \mu V.cm^{-1}$, to be equal to 250 A, from which the transition current I_q can be evaluated higher than 270 A.

The evolution of the critical current density J_c for both the uncoated and coated wires is displayed in Figure 11.a. As expected, J_c decreases as the magnetic field increases, but the same evolution is observed for both coated and uncoated samples, which means that the slight disturbance initiated by the ceramic coating onto the copper matrix, does not extend to the superconducting material. A similar observation was done when N-values deduced from eq.(8),

were compared for the uncoated and the coated strands (Figure 11.b). N is the signature of the resistive transition, deduced from the first derivative of the $V(I)$ curve at the critical current. If the superconductor is ideal, the curve will switch from horizontal to vertical, and N is infinite. As a result, a high value of N is the fingerprint of a high quality superconductor wire. Comparison between the uncoated and coated VAMAS reels shows that the N-values are in the same range, which confirms that the ceramic sheath has no influence on the superconducting properties of the Nb_3Sn wires. A slight reduction of the N-value for both reels reveals that the Nb_3Sn strands used for these experiments, were not of the highest quality, but, as the same behavior is observed for both the un-coated and coated Nb_3Sn strands, under high magnetic fields, this means clearly that it results from the intrinsic performances of the strand instead of the coating itself (Oh et al., 2007).
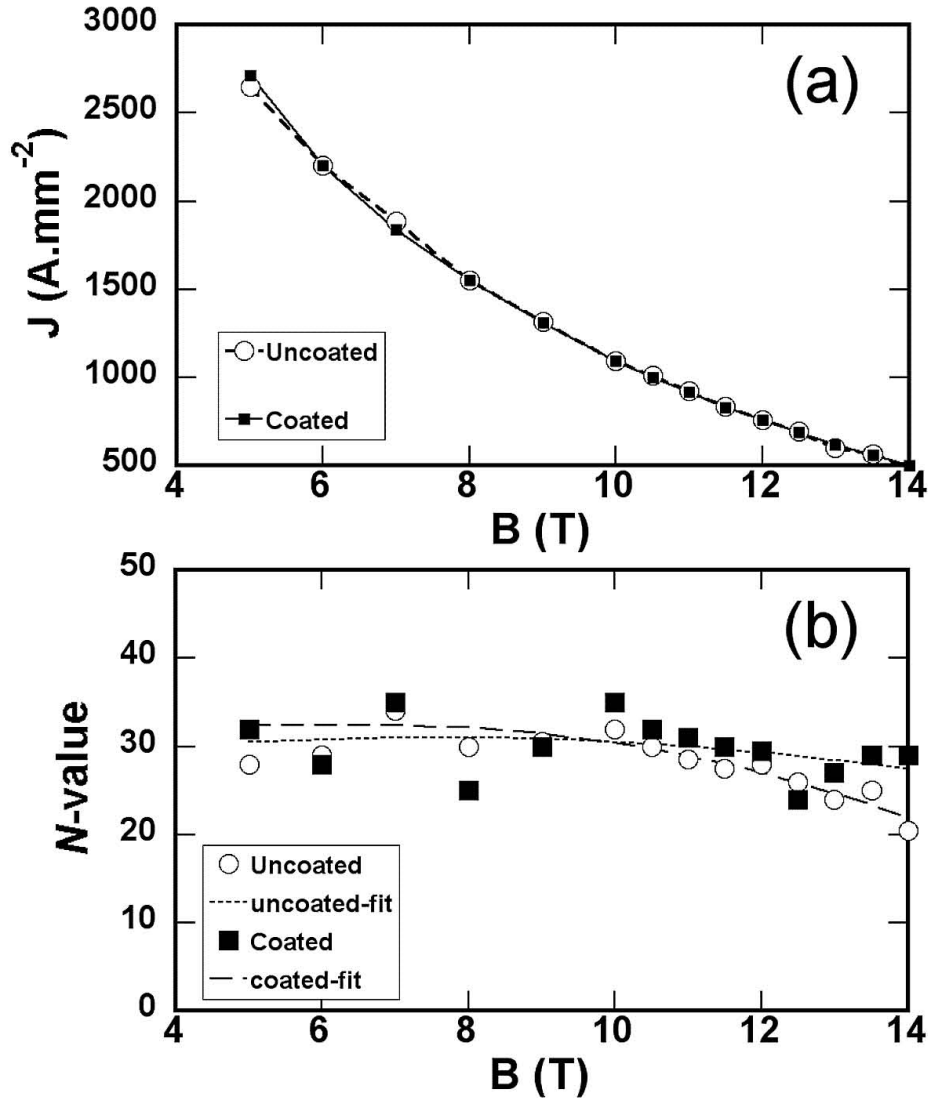
Figure 11: Evolution of (a) the critical current density J_c, and (b) the N-value, as a function of the magnetic field (lines: second degree polynomial fits of the experimental N values).

3.8. Electrical properties of the demonstrator

3.8.1. Critical current

The evolution of the electric potential of the demonstrator as a function of the applied current, was measured with an external magnetic field of 12 T (T = 4.2K), applied either with the (+I), or the (-I) configuration (Figure S5). An example of the resulting curves is reported in Figure S18:

with a (+I) configuration, the quenching current is equal to 167 A for $B_{max} = B_{CétacéS} = 12$ T, and

for the (-I) configuration, the quenching current is equal to 178 A for $B_{max} = B_{CétacéS} + B_{Reel} =$

$11.0 + 0.92 = 11.92$ T. All results are displayed in Table SIII. The variation of the quenching

current as a function of the magnetic field for the demonstrator (+I and -I configuration) was

compared with that of the strand alone (uncoated and coated) (Figure S19), and no major

difference was found between the response of the strand alone and that of the demonstrator. This

illustrates that the ceramic insulation does not affect the collective properties of the Nb_3Sn

superconducting strands. The value of the magnetic field induced by the reel alone ($B_{CétacéS} = 0$

T), when a 740 A current was applied, was equal to $B_{Reel} = 3.8$ T.

3.8.2. Operating mode

The evolution of the potential U generated in the demonstrator as a function of the applied

current, for centripetal (+I) and centrifugal (-I) forces (Figure S5), is reported in Figure 12. U

depends on the direction and variation of the intensity as a function of time, according to:

$U = L. (dI/dt)$ (9)

when L is the inductance of the reel (in Henry). Each measurement was reproduced three

times and led to the same results without any modification of the demonstrator properties.
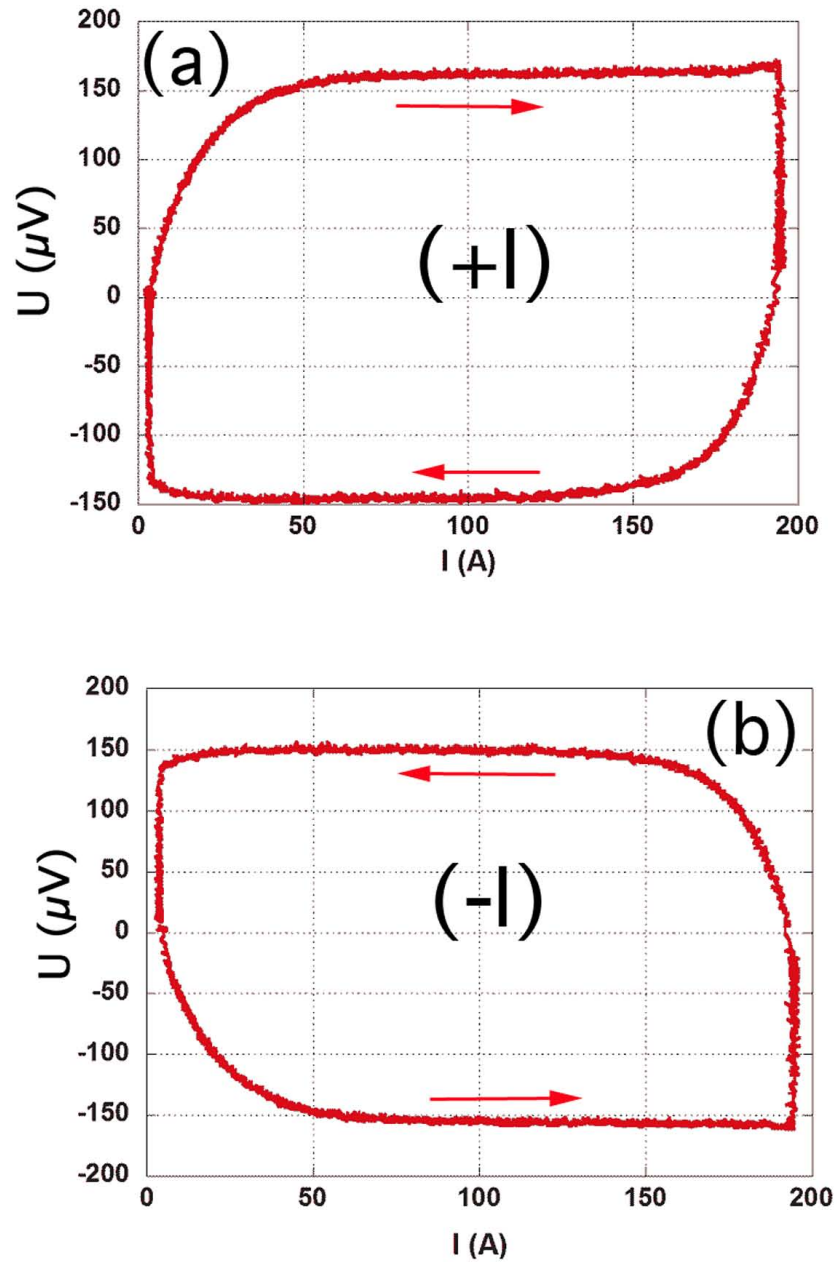
Figure 12. Curves U=f(I) for the demonstrator, for an external magnetic field $B_{CétacéS} = 11$ T, and a current varying between 0 and 194 A in the reel: (a) (+I) configuration, (b) (-I) configuration.

The evolution of the potential as a function of the variation of the applied intensity is symmetrical with both increasing and decreasing current intensities. First, as the current increases, a transient state is observed up to I = 50 A, (Figure 12.a, top curve) with a logarithm

evolution up to U = 150 μV, before reaching a constant value for the potential U, in agreement with eq. (9), up to I = 194 A. Once the current is stabilized (dI/dt = 0), U returns to 0. Reducing the current induces a parallel evolution but with a negative potential (dI/dt<0) (Figure 12.a, bottom curve). A similar, but opposite in sign, evolution was observed with the (-I) configuration (Figure 12.b). These analyses demonstrate that the ceramic sheath applied to the superconducting wire working under operating conditions, with a high external magnetic field and a high intensity current flowing through, can stand correctly the stress created by the induced Lorentz forces. In addition, the ceramic protection tested in this demonstrator, remains rigid and no fluctuation was observed neither in the U=f(I) curves, nor among these curves after several tests, which could have resulted from a rearrangement of the reel strands, if the ceramic coating could not constrain the superconducting strands.

CONCLUSION

The present study has demonstrated that flexible organic-free ceramic ribbons can be prepared by a method that allows for large-scale production. These ribbons can be stored for further use, and they contain a low temperature sintering frit that favors ceramization at low temperature under neutral atmosphere. These properties were obtained thanks to the specific properties of clay minerals, especially the Expans Mt that provides unique thixotropic properties.

These ceramic ribbons, which had been designed for a specific application in the domain of new Nb_3Sn-based superconducting wires, have been tested for this application, and the material has fulfilled all mechanical, electrical, and magnetic requirements, with no damage to the intrinsic properties of the superconducting stands.

Finally, the full integration of the ceramic protection with the superconducting material was validated with the assembling of a demonstration reel made with 20 meters of Nb_3Sn wires. This demonstrator could resist to the mechanical constraints induced by a 12 T external magnetic field, and a maximum current of 194 A could flow through without any damage. The testing reel itself could generate a 3.8 T magnetic field under supercritical conditions, with a 740 A applied current intensity. It appears that the oldest raw material manufactured by human being, can still find applications in the most advanced and sophisticated technology.

References

Ashkin, M. and J. R. Gavaler, 1978. Stability of Nb-Based, High-Tc A15 Componnds. Journal of Low Temperature Physics 31, 285-293.

Boutboul, T., A. den Ouden, et al. (2008). Nb3Sn conductor development and characterization for NED. 8th European Conference on Applied Superconductivity. S. Hoste and M. Ausloos. Bristol, Iop Publishing Ltd. **97**.

Breschi, M., L. Trevisani, et al., 2009. Comparing the thermal stability of NbTi and Nb3Sn wires. Superconductor Science & Technology 22

Canfer, S., G. Ellwood, et al., 2008. Insulation development for the Next European Dipole. IEEE Transactions on Applied Superconductivity 18, 1387-1390.

Caspi, S., D. Dietderich, et al., 2007. Fabrication and test of TQS01 - A 90 mm Nb3Sn quadrupole magnet for LARP. IEEE Transactions on Applied Superconductivity 17, 1127-1125.

Devred, A., 2002. Insulation systems for Nb3Sn accelerator magnet coils manufactured by the wind & react technique. IEEE Transactions on Applied Superconductivity 12, 1232-1237.

Devred, A., B. Baudouy, et al., 2006. Overview and status of the Next European Dipole Joint Research Activity. Superconductor Science & Technology 19, S67-S83.

Devred, A., D. E. Baynham, et al., 2004. High field accelerator magnet R&D in Europe. IEEE Transactions on Applied Superconductivity 14, 339-344.

Devred, A., T. Bush, et al. (1992). Review of SSC dipole magnet mechanics and quench performanc. New York, Plenum Press Div Plenum Publishing Corp.

Devred, A., S. A. Gourlay, et al., 2005. Future accelerator magnet needs. IEEE Transactions on Applied Superconductivity 15, 1192-1199.

Dew-Hughes, D., 1975. Superconducting A-15 compounds: A review. Cryogenics 15, 435-454.

Echarri, A. and M. Spadoni, 1971. Superconducting Nb3Sn: A review. Cryogenics 11, 274-284.

Felice, H., A. Mailfert, et al., 2007. Magnetic and mechanical design of a 130 mm aperture Nb3Sn dipole magnet. IEEE Transactions on Applied Superconductivity 17, 1047-1050.

Ferracin, P., G. Ambrosio, et al., 2007. Assembly and tests of SQ02, a Nb3Sn racetrack quadrupole magnet for LARP. IEEE Transactions on Applied Superconductivity 17, 1019-1022.

Godeke, A., 2006. A review of the properties of Nb3Sn and their variation with A15 composition, morphology and strain state. Superconductor Science & Technology 19, R68-R80.

Gould, D. and H. Wada, 1995. VAMAS - Introduction. Cryogenics 35, S7-S8.

Hafalia, A. R., S. Caspi, et al., 2005. Structure for an LHC 90 mm Nb3Sn quadrupole magnet. IEEE Transactions on Applied Superconductivity 15, 1444-1447.

Hulm, J. K. and B. T. Matthias, 1980. High-Field, High-Current Superconductors. Science 208, 881-887.

Kunzler, J. E., 1961. Superconductivity in High Magnetic Fields at High Current Densities. Review on Modern Physics 33, 501-509.

Loveridge, P., D. E. Baynham, et al., 2008. Mechanical Design of the Next European Dipole. IEEE Transactions on Applied Superconductivity 18, 1487-1490.

Matthias, B. T., T. H. Geballe, et al., 1963. Superconductivity. Review on Modern Physics 35, 1-22.

Matthias, B. T., T. H. Geballe, et al., 1954. Superconductivity of Nb3Sn. Physical Review 95, 1425-1435.

Miyazaki, T., T. Miyatake, et al., 2008. Development of Nb3Sn superconducting wires for high field magnets at Kobe Steel and JASTEC. Cryogenics 48, 341-346.

Muller, J., 1980. A15-type superconductors. Reports on Progress in Physics 43, 641-687.

Nobrega, F., N. Andreev, et al., 2008. Nb3Sn accelerator magnet technology scale up using cos-theta dipole coils. IEEE Transactions on Applied Superconductivity 18, 273-276.

Nobrega, F., A. V. Zlobin, et al., 2007. Nb3Sn Accelerator Magnet Technology Scale Up Based on Cos-Theta Coils. IEEE Transactions on Applied Superconductivity 17, 31-34.

Oh, S., C. Lee, et al., 2007. Field dependence of the n-value and its relation with the critical current of Nb3Sn strands. Superconductor Science & Technology 20, 851-858.

Summers, L. T., M. W. Guinan, et al., 1991. A model for the prediction of Nb3Sn critical current as a function of field, temperature, strain, and radiation damage. IEEE Transactions on Magnetics 27, 2041-2044.

Van Kessel, A. T., H. W. Myron, et al., 1978. On the electronic structure of A15 materials. Journal of Less Common Metals 622, 49-58.

Warnes, W. H. and D. C. Larbalestier, 1986. Critical current distributions in superconducting composites. Cryogenics 26, 643-653.

Zlobin, A. V., G. Ambrosio, et al., 2005. Development and test of Nb3Sn cos-theta dipoles based on PIT strands. IEEE Transactions on Applied Superconductivity 15, 1160-1163.

Supplementary Material

Organic free montmorillonite-based flexible insulating sheaths for Nb$_3$Sn superconductor magnets.

Eric Prouzet*, Alexandre Puigségur, André Larbot, Jean-Michel Rey, Françoise Rondeaux
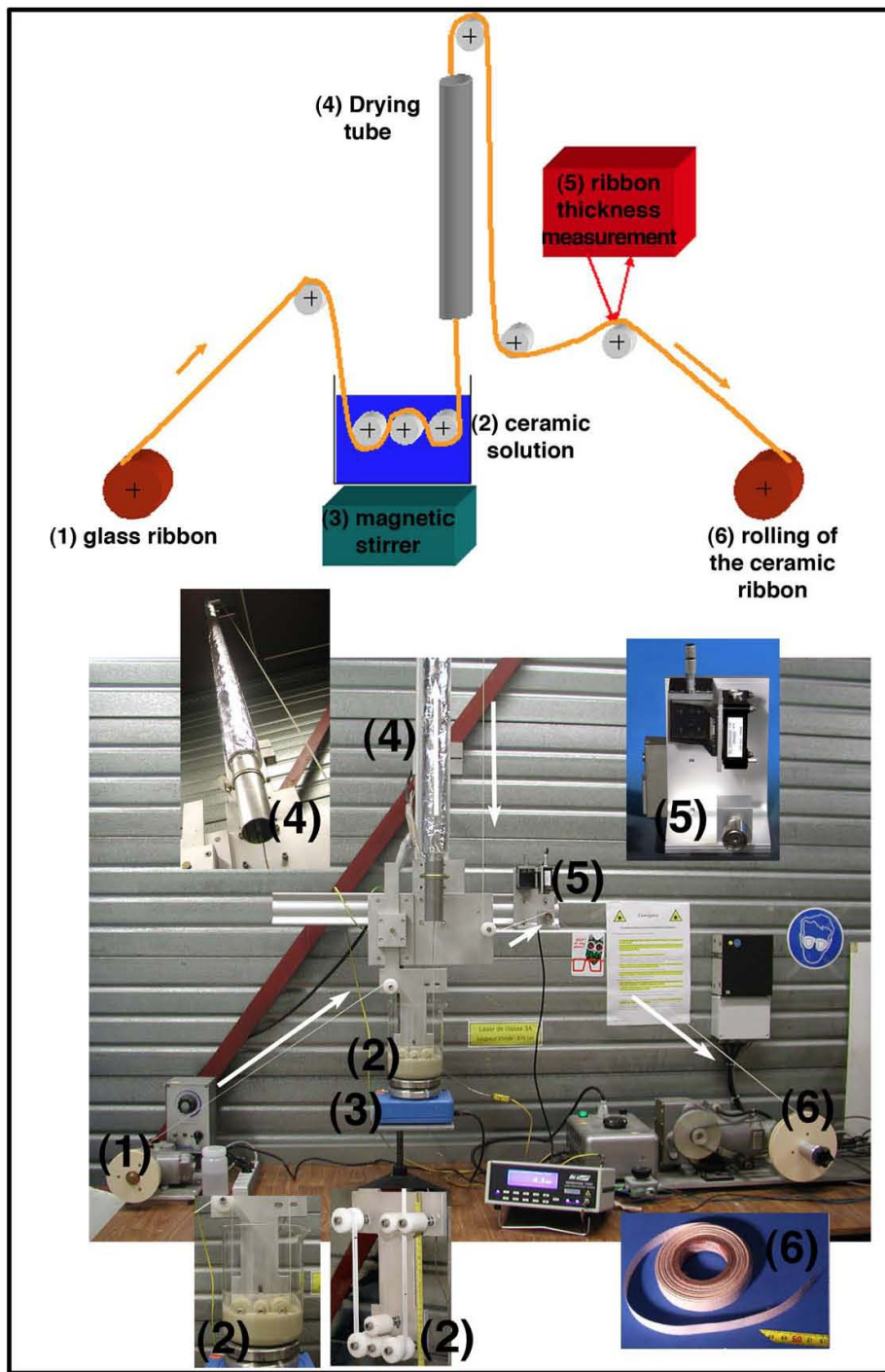
Figure S1. Schematic (top) and photo (bottom) of the impregnation bench.
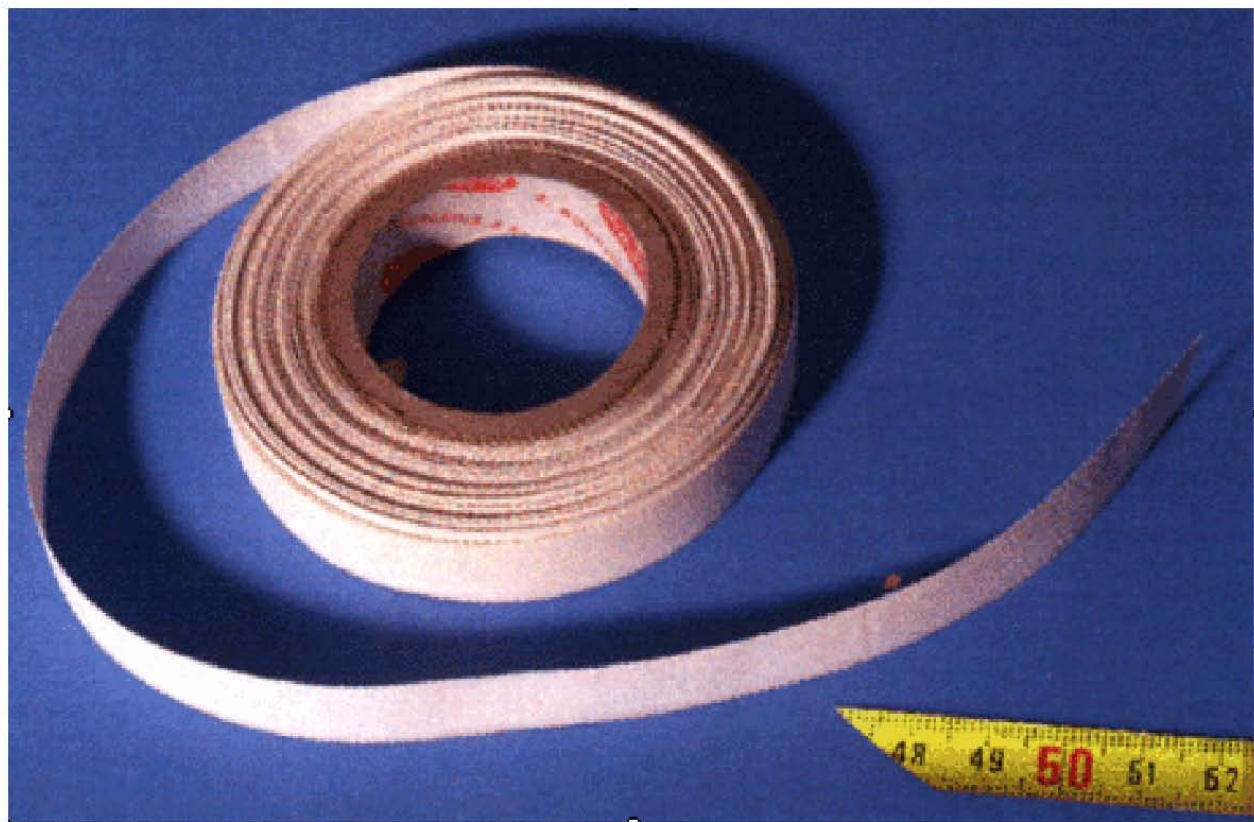
Figure S2. Ceramic ribbon prepared by the impregnation of a glass fiber ribbon by an organic-free ceramic aqueous dispersion.
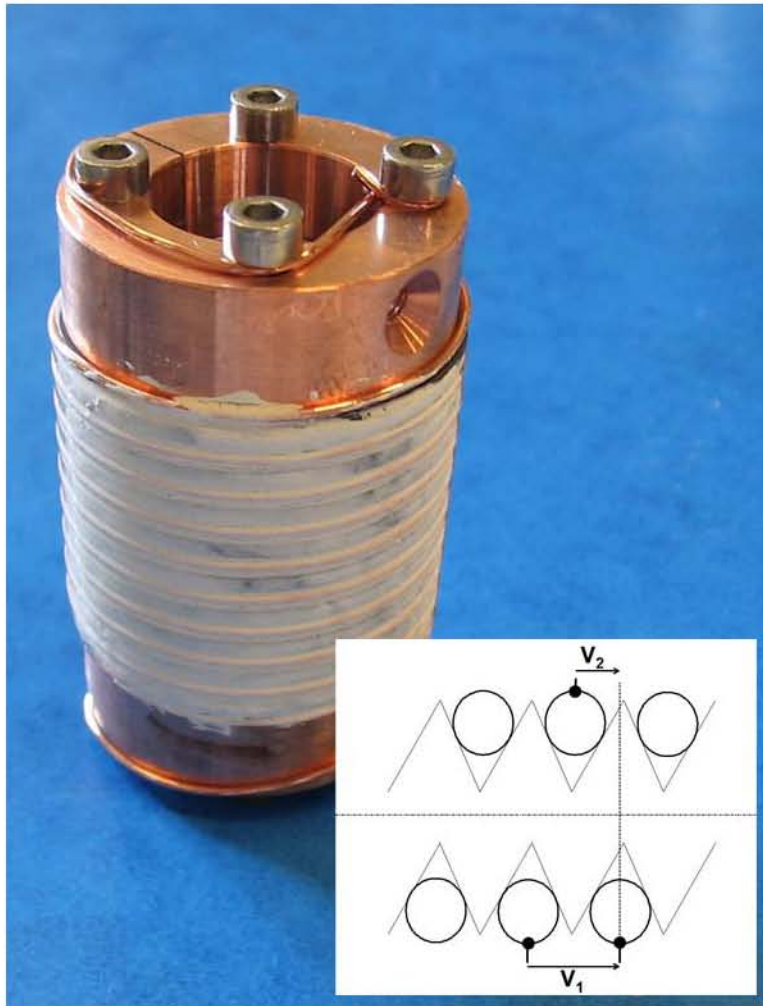
Figure S3: VAMAS reel used for the critical current tests. Insert: scheme of the two potential measurement points

Figure S4: (left) CétacéS power station for the measurement of superconductors under a high magnetic field and at low temperature; (b) close view of the measurement stick that is inserted into the cryostat: the VAMAS sample is located at the bottom and the electrical current is provided by an over-dimensioned copper stick to avoid any Joule effect.
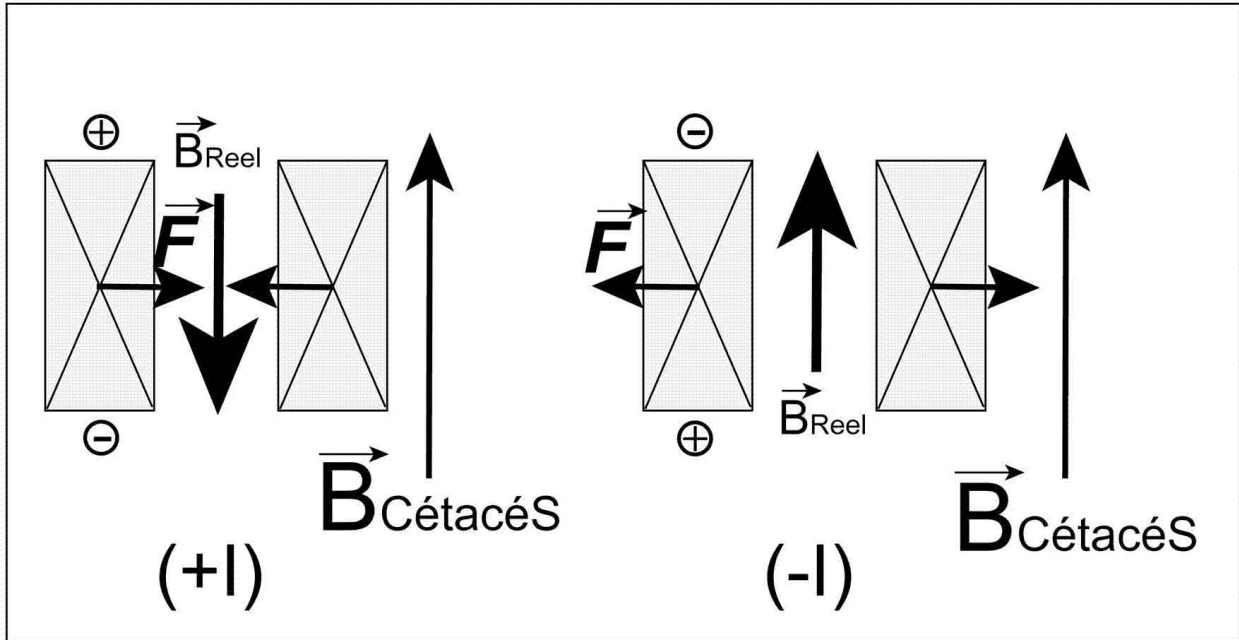
Figure S5: Schematic of the different magnetic fields and forces generated in the testing reel, as a function of the current direction: (+I) creating centrifugal forces; (-I) creating centripetal forces. The external magnetic field $B_{CétacéS}$ remains constant, and the induced magnetic field B_{Reel} resulting from the current flowing through the testing reel, can be either antiparallel (+I) or parallel (-I) to the external field.
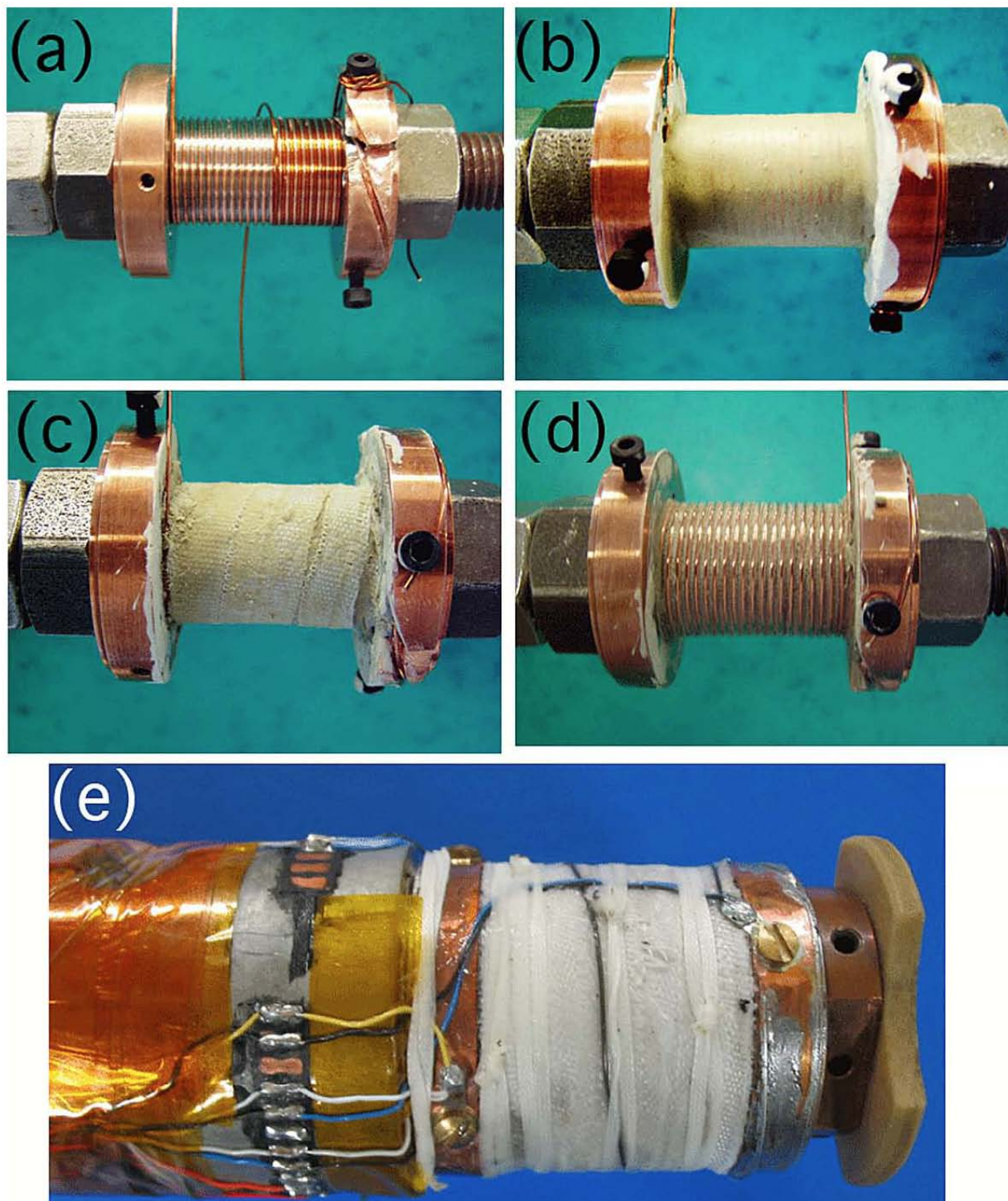
Figure S6: Assembling steps of the test reel for magnetic measurements: (a) first strand reeled , (b) application of the ceramic gel, (c) application of the ceramic ribbon, (d) second strand reeled, (e) final testing reel connected to the CétacéS sample holder.
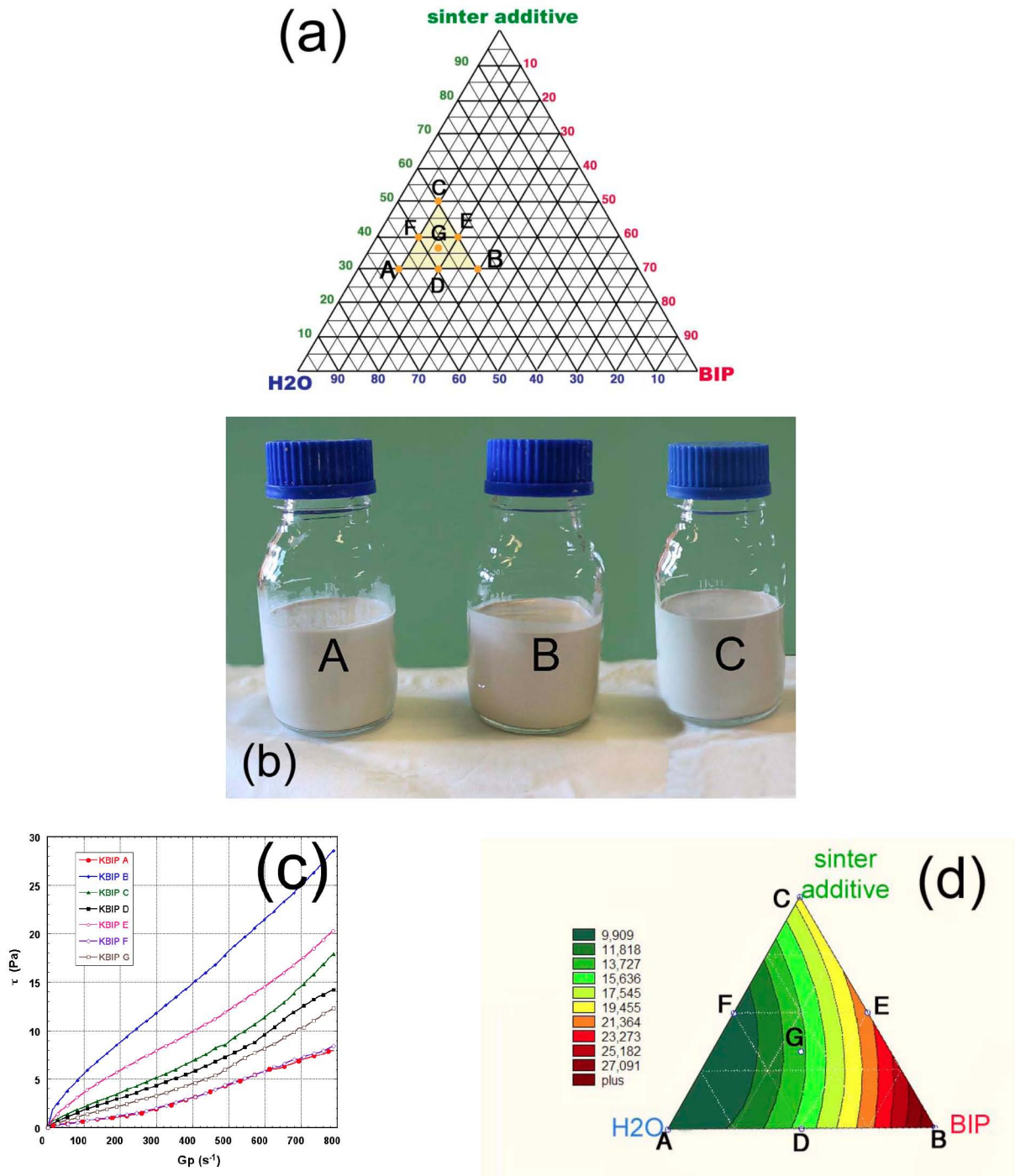
Figure S7: Rheological results for BIP™ : (a) phase diagram; (b) samples after stirring; (c) strain τ as a function of the spinning speed Gp; (d) viscosity map within the sample area.
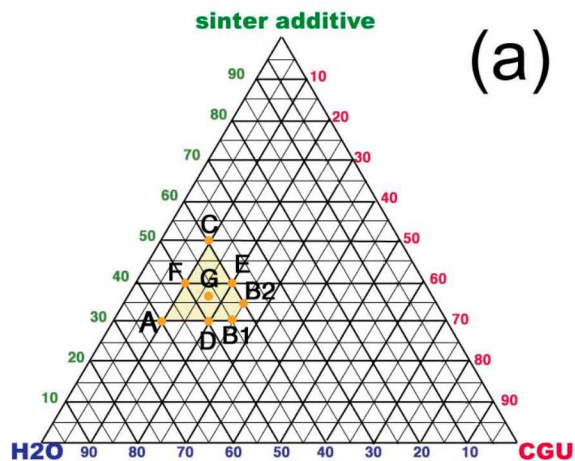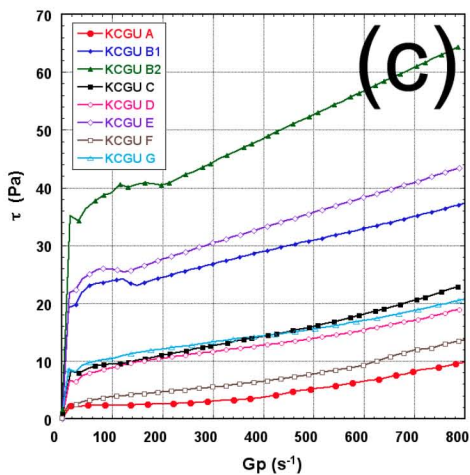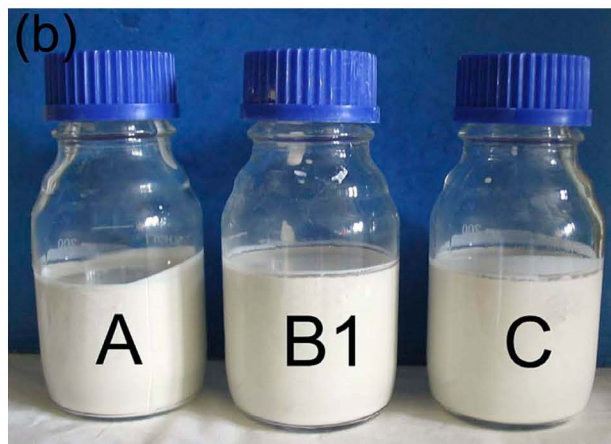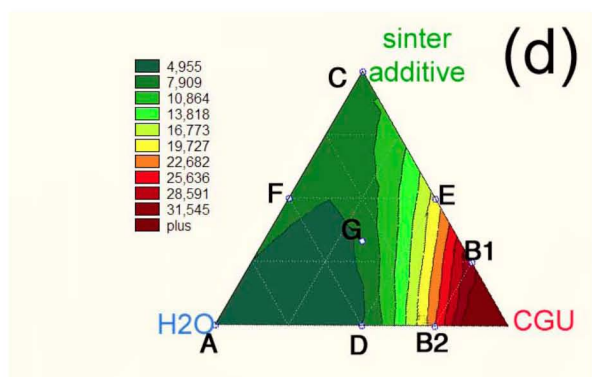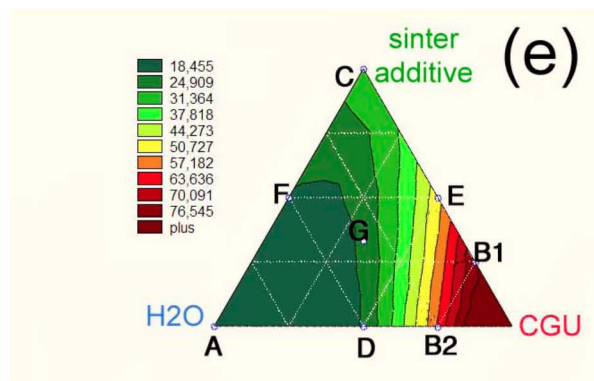
Figure S8: Rheological results for CGU™: (a) phase diagram; (b) samples after stirring; (c) strain τ as a function of the spinning speed Gp; viscosity map within the sample area for spinning speed of (d) 100 cm.s⁻¹ and (e) 600 cm.s⁻¹.
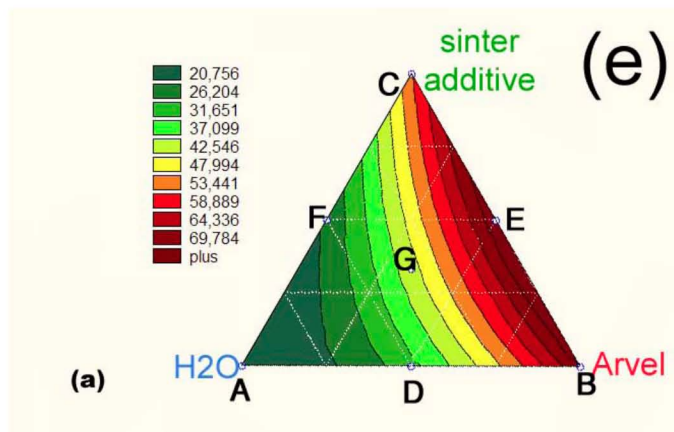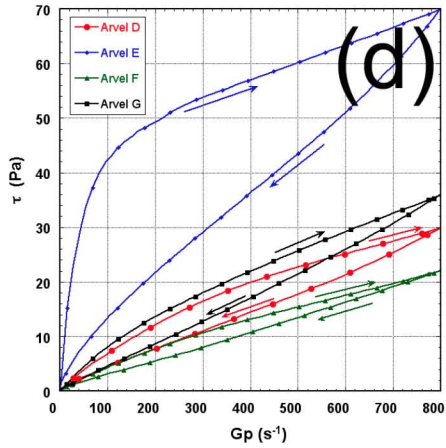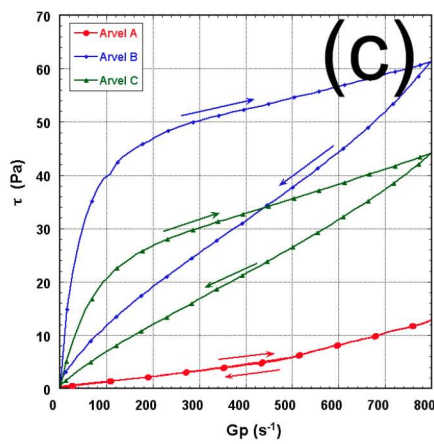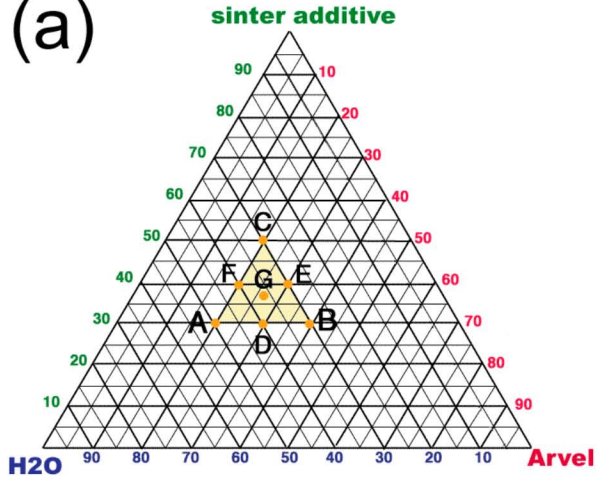
Figure S9: Rheological results for the Arvel™ : (a) phase diagram; (b) samples after stirring; (c,d) strain τ as a function of the spinning speed Gp; (e) viscosity map within the sample area calculated at Gp = 300cm.s^{-1}.
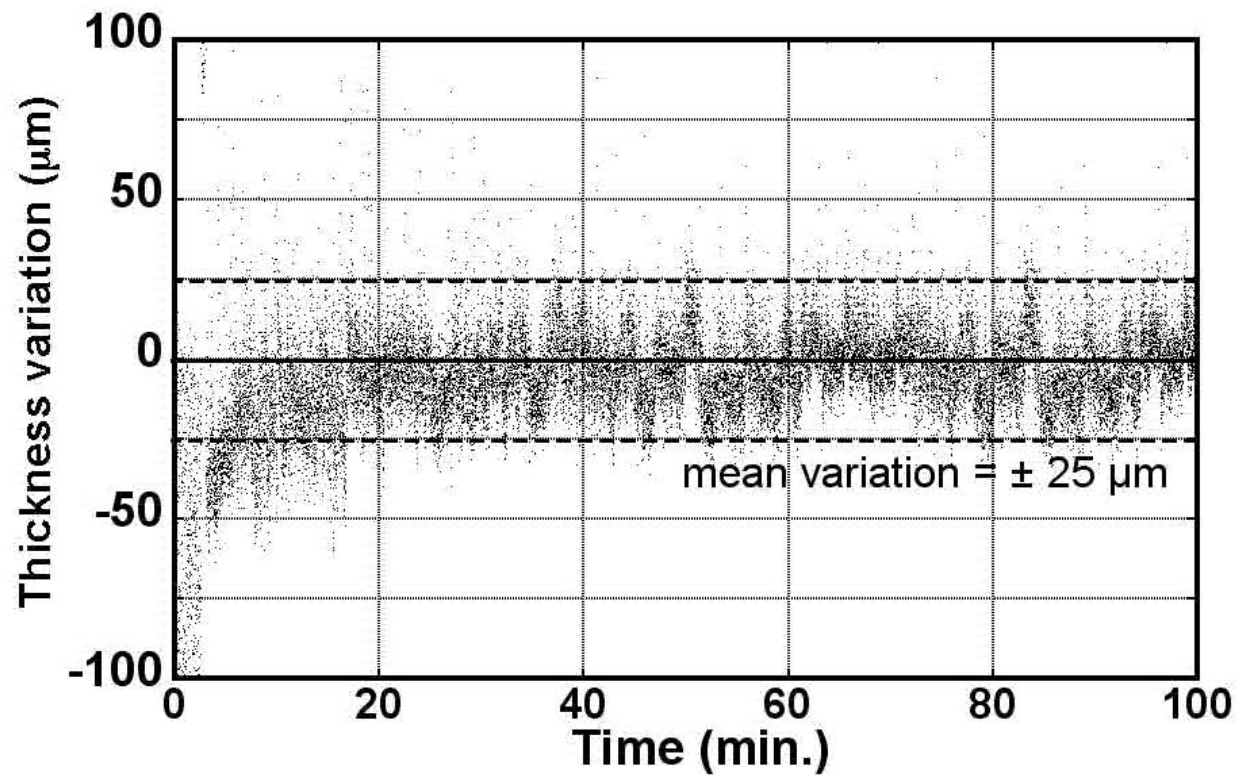
Figure S10: Average variation of the thickness of the crude ribbon after impregnation and drying of the ceramic suspension around the mean value (200 μm). coating rate: 30 cm.sec^{-1}.
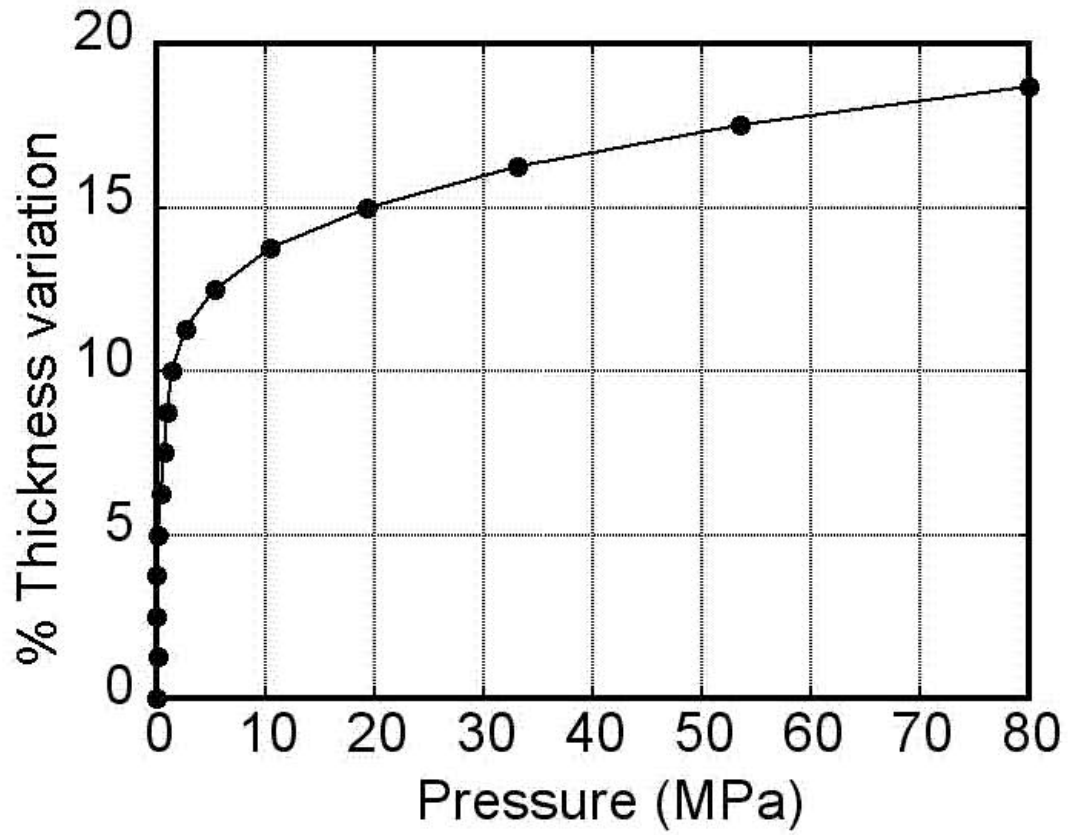
Figure S11: Evolution of the thickness of crude ceramic ribbons as a function of the applied load
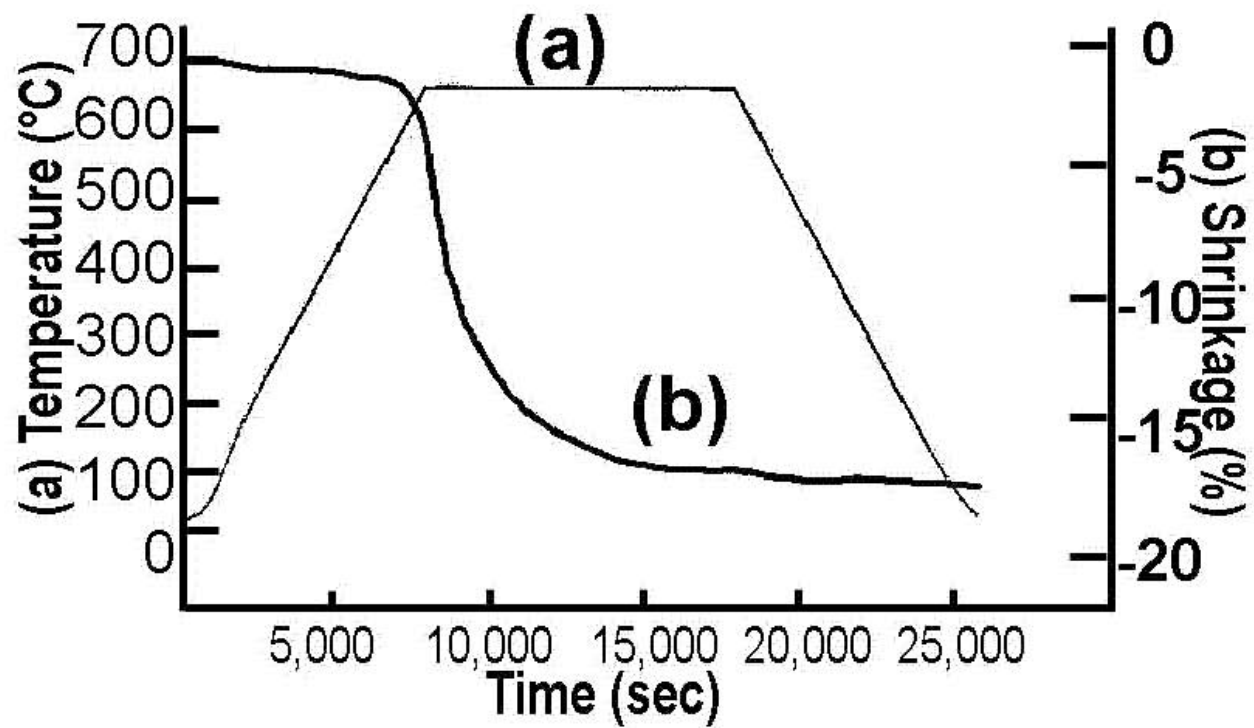
Figure S12: Dilatometry analysis of a ceramic pellet prepared with the J2 composition

Figure S13: Evolution of the ceramic pellets as a function of the thermal treatment. From top to bottom: as-prepared, 600°C, 720°C. See Table II for compositions
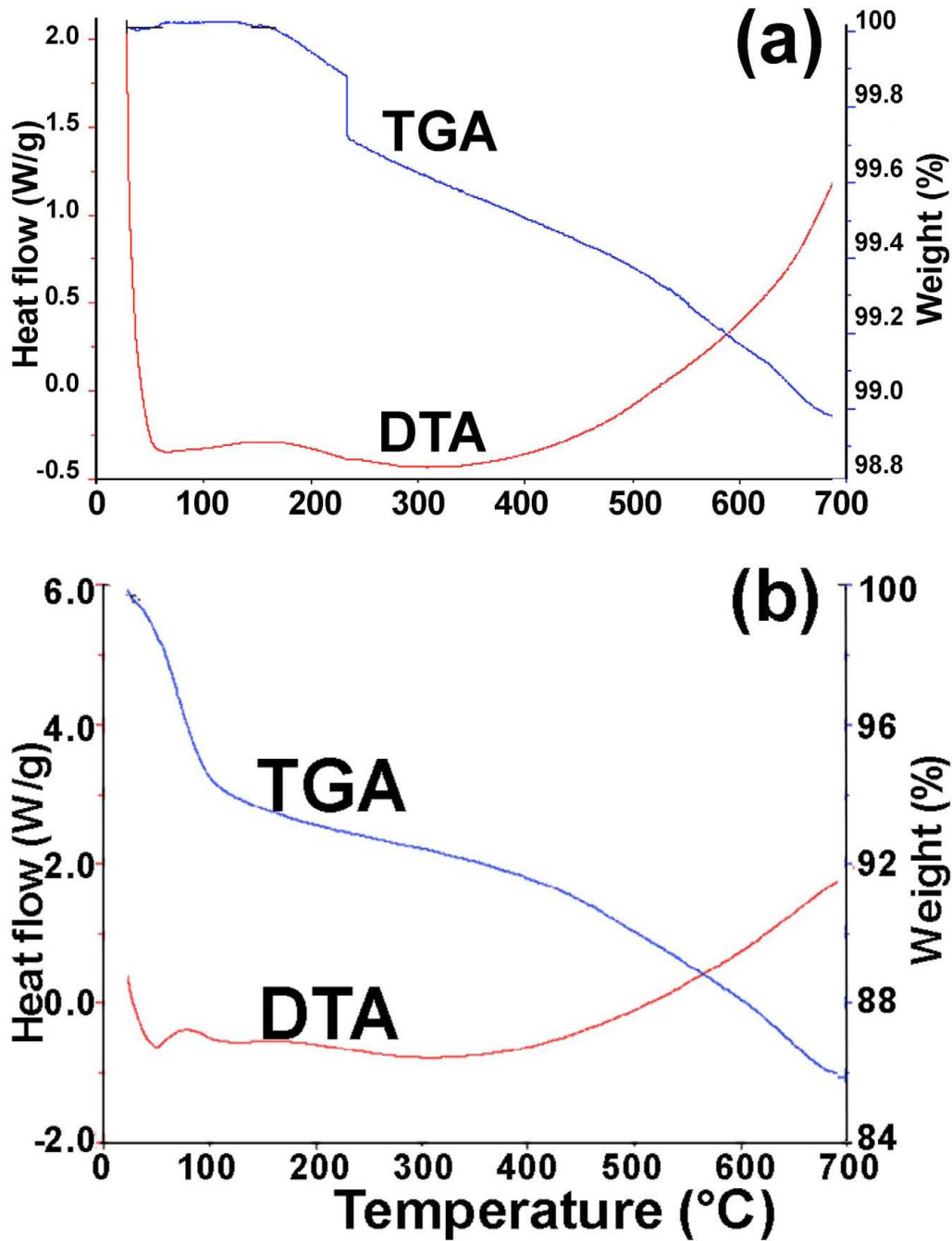
Figure S14: DTA-TGA analysis of (a) the sintering fritt, and (b) the Expans™ montmorillonite.
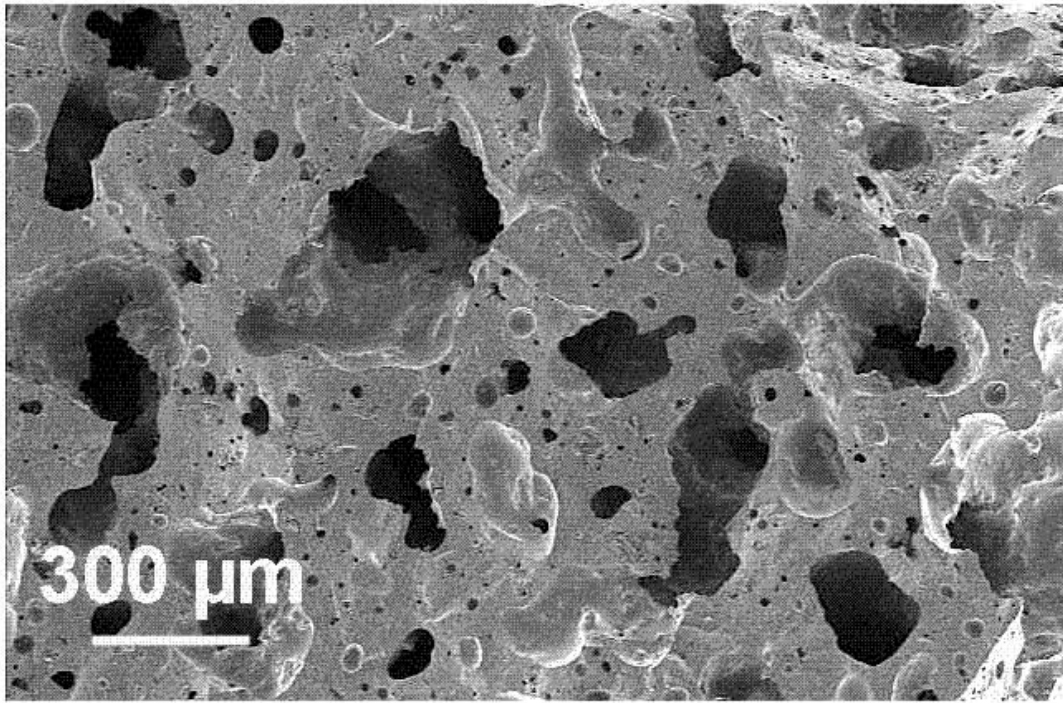
Figure S15: SEM observation of a pellet made of a sample J3 (Table SII) sintered at 660°C.
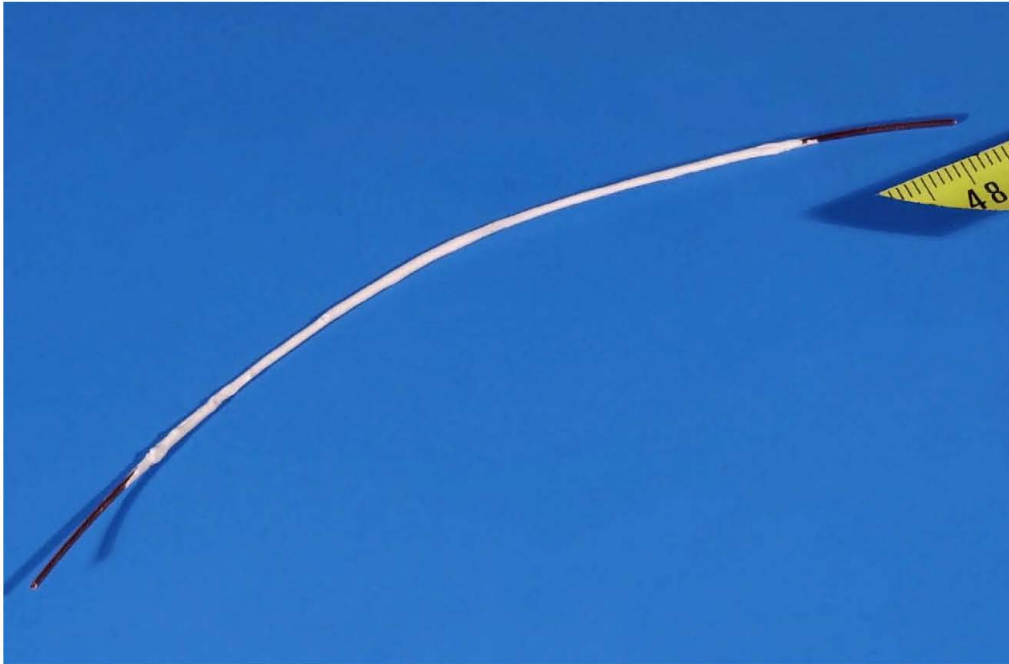
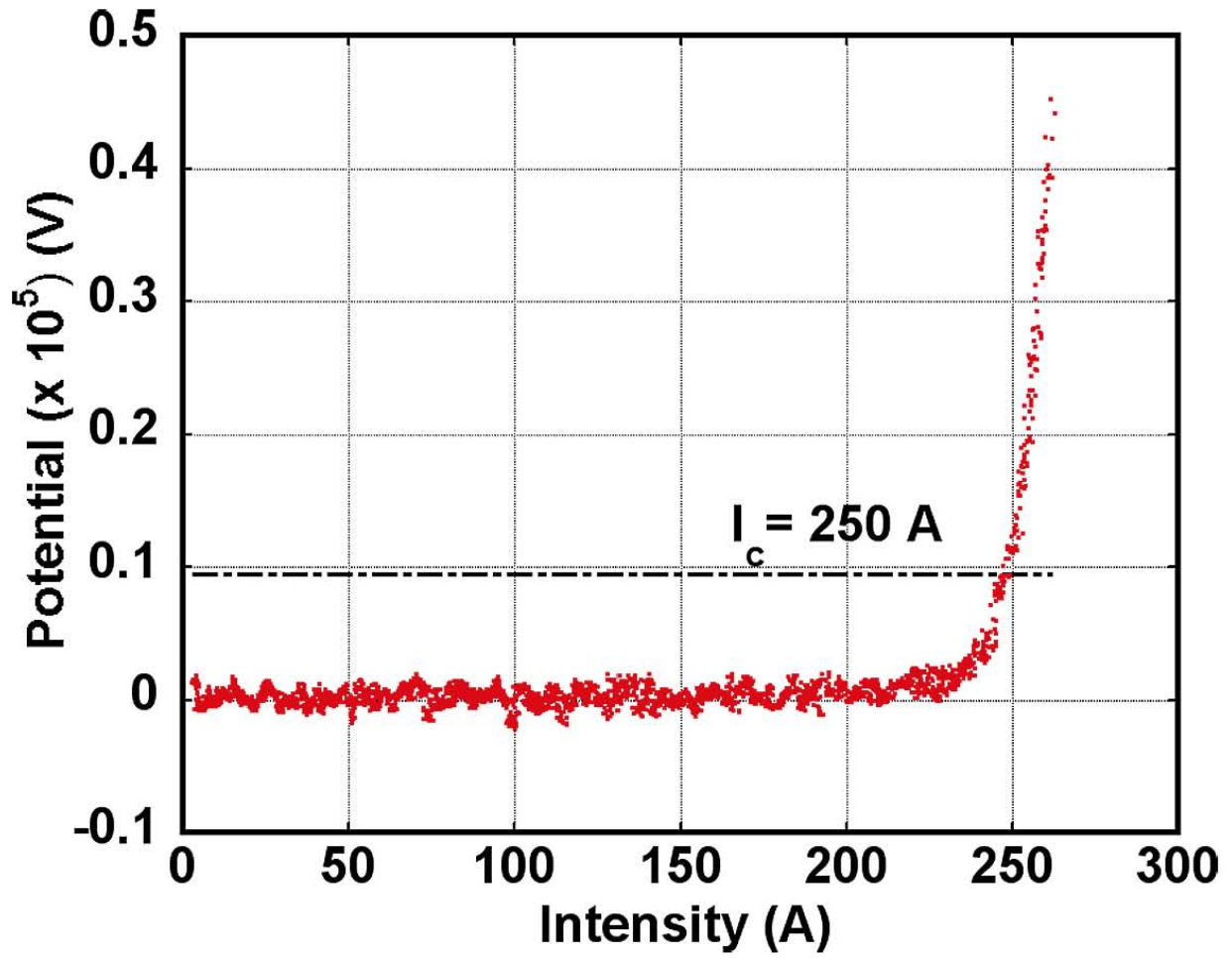Figure S16: Photo of a Nb$_3$Sn/Cu wire used for the RRR measurements

Figure S17: Determination of the critical current I_c based on the apparent electrical field parameter E_{sc}, under a magnetic field of 10 T.
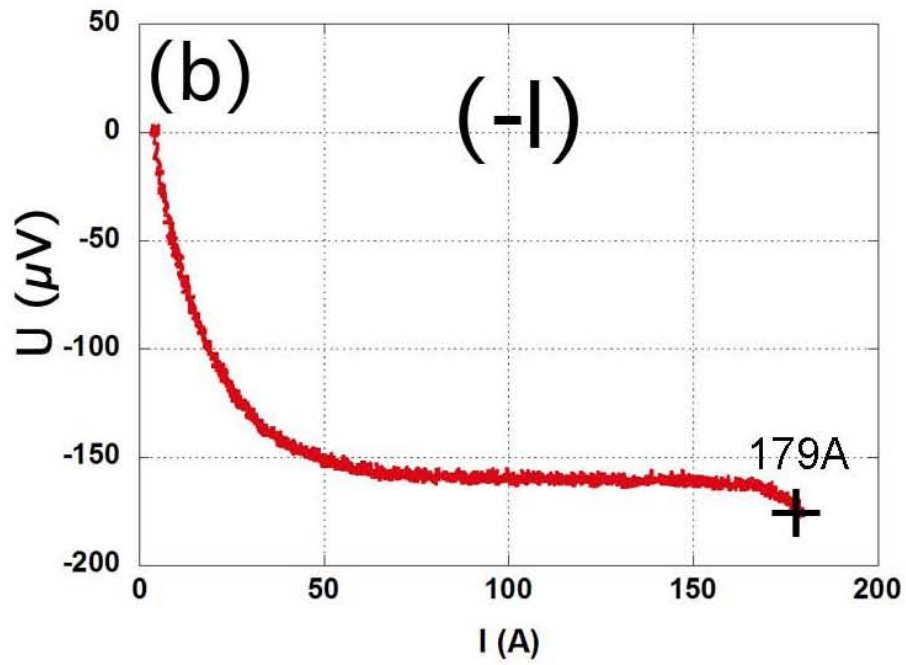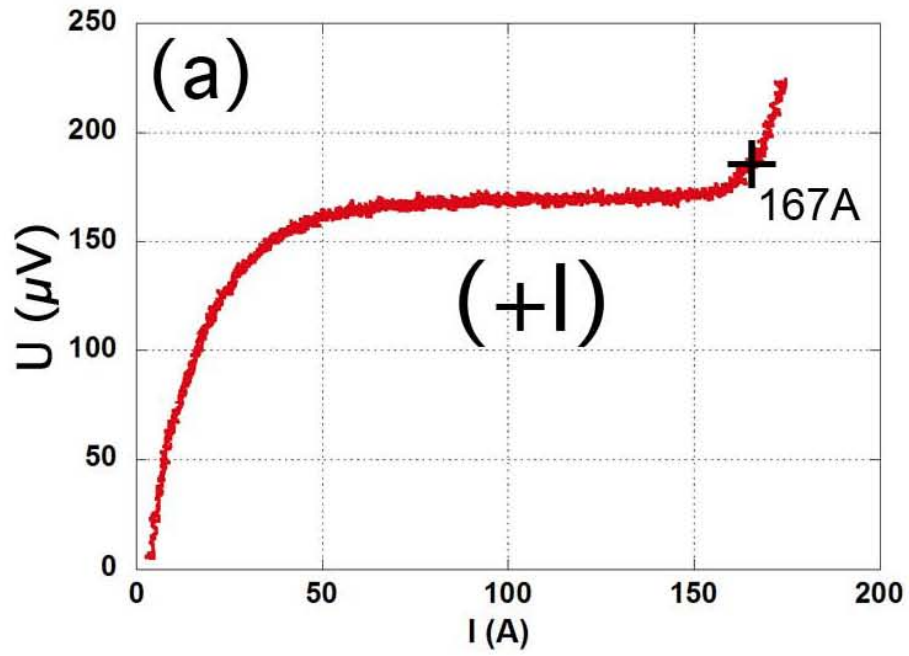
Figure .S18. Curves U=f(I) obtained with the demonstrator, with the current being increased until a quenching is observed (marked by a variation of U=(f(I): (a) (+I) configuration, (b) (-I) configuration.
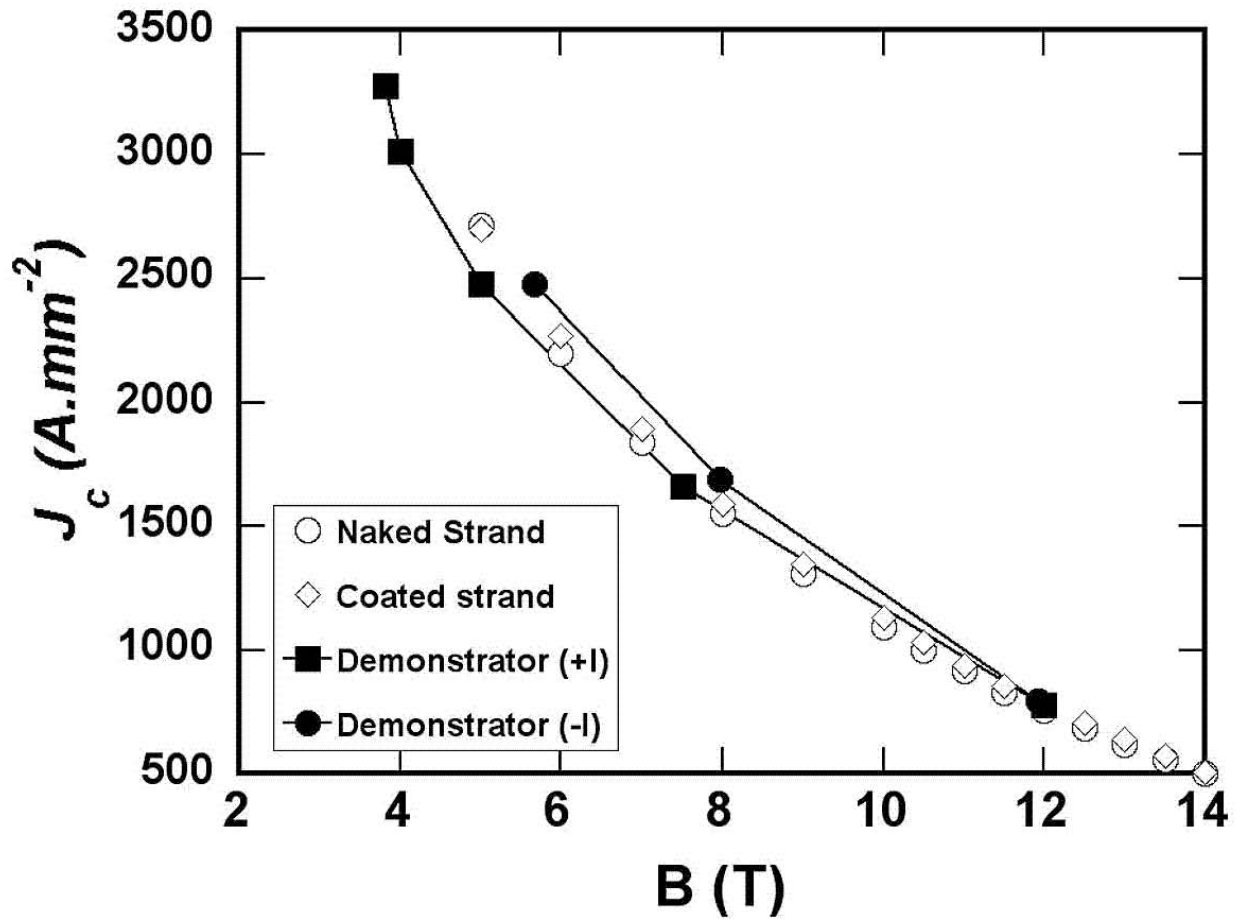
Figure S19: Comparison of the critical (quenching) current density measured with the demonstrator (+I & -I) as a function of the external magnetic field, with those measured with the superconducting strand alone, and after coating with the ceramic suspension.

Table SI. Compositions of the different mixtures tested for rheology

Sample	water (wt%)	sinter agent (wt%)	Clay (wt%)	S/Ms*
A	60	38	2	0.95
B	60	30	10	0.75
C	40	50	10	0.83
D	40	58	2	0.97
E	45.5	50	4.5	0.92
F	52.5	40	7.5	0.94
G	55	40.5	4.5	0.9
H	45	47.5	7.5	0.86
I	48	50	2	0.96

* S/Ms: mass of sinter agent over total mass of the solid phase

Table SII. Compositions of the different mixtures tested for sintering

Sample	clay (wt%)	sinter agent (wt%)	S/Ms*
J1	40	60	0.6
J2	30	70	0.7
J3	25	75	0.75
J4	20	80	0.8
J5	10	90	0.9

* S/Ms: mass of sinter agent over total mass of the solid phase

Table SIII. Quenching currents and maximum stress observed under various magnetic fields.

Current Direction	I_{quench} (A)	J_{quench} (A.mm^{-2})	$B_{CétacéS}$ (T)	B_{Reel} (T)	B_{max} (T)	Stress (MPa)
(+I)	740	3.8	0	3.8	3.86	18.96
(+I)	680	3.5	4	3.5	4.51	20.35
(+I)	559	2.9	5	2.9	5.42	20.11
(+I)	375	1.9	7.5	1.9	7.8	13.57
(+I)	175	0.9	12	0.9	12.19	14.16
(-I)	2478	2.97	2.5	2.97	5.42	20.11
(-I)	1693	1.96	6	1.96	8.0	20.3
(-I)	794	0.92	11	0.92	11.95	14.2

* S/Ms: mass of frit over total mass of the solid phase